The Role Of Circle Of Willis Anatomy Variations In Cardio-embolic Stroke - A Patient-specific Simulation Based Study

Debanjan Mukherjee *[1], Neel D. Jani †[1], Jared Narvid ‡[2,3], and Shawn C. Shadden §[1]

[1]Dept. of Mechanical Engineering, University of California, Berkeley
[2]Radiology and Biomedical Imaging, University of California, San Francisco
[3]Zuckerberg San Francisco General Hospital and Trauma Center

Abstract

Despite available clinical evidence, several underlying issues regarding the connection between Circle of Willis anatomy and stroke remain unclear. Embolisms comprise a major cause of ischemic stroke, and discerning how emboli traverse the complex cerebral arterial network is challenging. Here we describe a patient-specific simulation based investigation on the role of Circle anatomy in cardioembolic stroke. Our simulation framework consists of medical image-driven modeling of patient anatomy including the Circle, simulation of 3D blood flow through patient vasculature, embolus transport modeling using a discrete particle dynamics technique, and a sampling based approach to incorporate parametric variations. Five Circle anatomical variants are identified using ranking statistics applied to occurrence frequency data in literature, for each variant. A total of 24 (four patients and six Circle anatomies including the complete Circle) models were considered, with cardiogenic emboli of varying sizes and compositions released virtually and tracked to compute distribution to the brain. The results establish that Circle anatomical variations significantly influence embolus distribution to the six major cerebral arteries. Embolus distribution to middle brain is found to be least sensitive to the influence of anatomical variations. For varying Circle topologies, differences in flow through cervical vasculature are observed. This incoming flow is recruited differently across the communicating arteries of the Circle for varying anastomoses. Emboli interact with the routed flow, and can undergo significant traversal across the Circle arterial segments, depending upon their inertia and density ratio with respect to blood. This interaction drives the underlying biomechanics of embolus transport across the Circle, explaining how Circle anatomy influences embolism risk.

Keywords: *Stroke; Embolus; Hemodynamics; Circle of Willis; Fluid-particle interaction*

*debanjan@berkeley.edu
†neelj@berkeley.edu
‡jared.narvid@ucsf.edu
§shadden@berkeley.edu

1 Introduction

The Circle of Willis (hereafter referred to as CoW) is a ring-like network of arteries in the brain, which conjoins the six major cerebral arteries, the internal carotid arteries, and the basilar artery. This network of vessels play a key role in maintaining cerebral blood flow distribution as flow enters from the internal carotids and the vertebro-basilar arteries, enabling collateral flow between hemispheres, and providing a compensatory collateral flow mechanism in case of flow disruption in one of the major supplying arteries [32, 13, 21]. The anatomy of the CoW manifests considerable variations among subjects, as documented in several studies [2, 4, 16]. Only about 40% of the population has a well-formed complete CoW anatomy while the remaining manifest some anatomical variations. The dominant anatomical differences are due to under-developed (hypoplastic) or absent (aplastic) artery segments, while fused vessels and additional vessel segments are also sometimes observed [4].

Given its key role in distributing blood and maintaining cerebral perfusion, the connection between CoW anatomy and ischemic stroke is of considerable interest. Prior studies have indicated that the proximal collateral circulation capabilities of the CoW plays an important role in the pathophysiology of cerebral ischemia [13, 23]. The anatomy of the CoW has also been linked to stroke risks in patients with occlusive internal carotid artery disease via medical imaging studies [33, 19, 15, 13, 14, 41]. For example, trans-cranial Doppler imaging in conjunction with carotid compression has been employed to characterize CoW collateral capability in [15, 13, 14], while MR imaging on patient population with reported stroke incidences have been used to explore the link between ischemia and CoW anatomy in [33, 41]. Majority of these investigations are clinical, based on imaging studies on patient cohorts, and the insights presented here are primarily based on compensatory hemodynamic flow through the communicating arteries.

It is well-known that a significant proportion of ischemic stroke and transient ischemic attack (TIA) are ultimately due to an embolus [9, 6], and CT or MR imaging of the occlusion location often fails to provide information on the source of the embolus causing the ischemia (leading to difficulty in diagnosis in the presence of multiple potential sources of embolisms) [10, 12]. This motivates investigating how CoW anatomy impacts cerebral embolic events. However, this has remained a major challenge since it is difficult to control for the anatomy of the CoW and model embolus dynamics in patient-cohort studies or animal models. Recent advances in medical image-driven computational modeling have opened up the possibility of addressing this challenge via systematic in silico studies on image-based vascular models[35, 38]. Specifically, flow in the CoW, and the influence of anatomical variations on hemodynamics, has been studied using one-dimensional reduced-order network models [1, 8], and using three-dimensional computational fluid dynamics simulations on representative CoW geometry [3].

In a series of prior works [7, 29, 28, 30], we have established a detailed computational pipeline for studying embolus transport in 3D patient-specific hemodynamics. Our computational model is composed of: (a) medical image-based modeling of vascular anatomy; (b) fully resolved 3D time-dependent flow simulations; (c) discrete particle method for embolus transport; and (d) a Monte-Carlo type approach for characterizing embolus distribution statistics. We have addressed mathematical modeling issues pertaining to embolus transport [29, 30], described how embolus size and other factors influence embolus distribution to the brain [7, 28], characterized differences between cardiogenic and aortogenic emboli in terms of their distribution in the brain [28], and demonstrated that understanding the chaotic advection of emboli through large arteries is necessary for discerning the source-destination relationship for cerebral emboli [30]. In this work, we seek to investigate the link between CoW anatomical variations and transport of emboli. The objective here is two-fold. The first objective is to test the hypothesis that the anatomy of CoW does influence embolus distribution in the brain. The second, is to describe a mechanistic reasoning for this influence based on hemodynamics.

2 Methods

2.1 Selection of anatomical variations for Circle of Willis

A broad literature search was performed for research articles comprising population data on the frequencies of the various CoW anatomical variations. A set of 25 research articles (reference list included in supplementary material) were selected from the search results. Frequencies of occurrence of the various commonly observed CoW anatomical variants were extracted from these articles. Using ranking statistics on the occurrence frequency data, a list of anatomical variations arranged in order of frequency was obtained. The 5 most frequent variations were chosen to be a part of this study. These involved an absent/hypoplastic anterior communicating artery (AcoA), left and right posterior communicating arteries (L.Comm, R.Comm), and left and right P1 (LP1, RP1) connectors (fetal type posterior cerebral artery anatomy). The respective complete CoW anatomy was also included in the study - resulting in a total of 6 anatomical variations of the CoW being studied per patient. Schematic representation of these anatomical variants have been presented on the top-row in Figure 1. The label for the various vessels have been described in Figure 1 which will be consistently employed throughout this paper. Namely, middle, anterior, and posterior cerebral arteries will be referred to as MCA, ACA, and PCA respectively. Internal carotid arteries, and basilar arteries will be referred to as ICA and BA respectively. Right and left are indicated by the suffix R and L.

2.2 Image-based modeling of anatomy

A set of four representative patient geometries was selected for this study, from amongst a larger set of computed tomography (CT) images acquired as a part of the Screening Technology and Outcome Project in Stroke (STOP-Stroke) database study [34]. All images were acquired under a protocol approved by the institutional review board as detailed in [34]. The patient anatomies were selected such that they possessed a complete CoW anatomy, and well differentiated branching vessels at the aortic arch (that is, no fused vessels or bovine arch anatomy). From the chosen CT images, artery lumen segmentations were generated using the custom 2D lofted image-segmentation technique incorporated in the open-source cardiovascular modeling package SimVascular [40]. During segmentation, it was ensured that cerebral vasculature up to the M1, A1, and P1 segments of the MCA, ACA, and PCA respectively, were included for each patient. The image segmentations were used to generate 3D computer solid models of the complete arterial pathway from the aorta to the CoW. In order to incorporate anatomical variations of the CoW within this image-based modeling procedure, respective communicating artery segmentations were iteratively detracted from the original segmented data, and the modified segmentations were re-lofted to generate 3D models of the corresponding incomplete CoW anastomoses. Note that for the purpose of this study, hypoplastic and aplastic segments are treated the same. By virtually introducing CoW variations in a given patient model (as opposed to a patient with that anatomical variant inherent) we could control against other inter-patient variabilities, and isolate the effect of CoW anatomy. Spanning across four patients, each with a total of six CoW topologies described in Section 2.1, a set of 24 anatomic models were thus created, which have been illustrated in Figure 1. Each model was thereafter discretized into a computational mesh for performing finite-element based hemodynamics simulations using SimVascular [40]. The average number of linear tetrahedral elements for each computational model ranged between 6.0-8.5 million, with average element size ranging between 0.36 mm and 0.52 mm, a choice that is guided by detailed mesh refinement and flow analysis studies as described in [22]. Further details on the modeling and meshing operations, as well as mesh refinement, have been discussed in prior studies [29, 30].

2.3 Hemodynamics simulation

For simulating the hemodynamic flow fields, blood was assumed to be a Newtonian fluid, with bulk density of 1.06 g/cc, and viscosity of 4.0 cP. Three-dimensional blood flow through each of the 24 anatomical models was modeled using the classical Navier-Stokes equations and continuity equation, describing momentum and mass balance, respectively, for blood flow. A Petrov-Galerkin stabilized linear finite-element method was employed to solve these equations for calculating flow velocity and pressure fields. The summary of equations, including the variational form for finite-element method, has been presented as follows:

$$\rho_f \left(\frac{\partial \mathbf{u}}{\partial t} + (\mathbf{u} \cdot \nabla \mathbf{u}) \right) = -\nabla p + \nabla \cdot \tau + \rho_f \mathbf{g} \tag{1}$$

$$\nabla \cdot \mathbf{u} = 0 \tag{2}$$

$$\tau = 2\mu_f \mathbf{D}(\mathbf{u}) = \mu_f \left(\nabla \mathbf{u} + \nabla \mathbf{u}^T \right) \tag{3}$$

$$\rho_f \left(\mathbf{w}, \frac{\partial \mathbf{u}}{\partial t} \right)_\Omega + \rho_f \left(\mathbf{w}, (\mathbf{u} \cdot \nabla) \mathbf{u} \right)_\Omega + 2\mu_f \left(\mathbf{D}(\mathbf{w}), \mathbf{D}(\mathbf{u}) \right)_\Omega - \rho_f \left(\mathbf{w}, \mathbf{b} \right)_\Omega - \left(\nabla \cdot \mathbf{w}, p \right)_\Omega - \left(\nabla q, \mathbf{u} \right)_\Omega + \left(q, \mathbf{u} \cdot \mathbf{n} \right)_\Gamma$$
$$- \underbrace{\left(\mathbf{w}, \mathbf{h} \right)_{\Gamma_t \ominus \Gamma_B}}_{\text{traction boundaries}} + \underbrace{\left(\mathbf{w}, \mathbf{h}_{0D} \right)_{\Gamma_B}}_{\text{outflow boundaries}} + \sum_{e=1}^{N_{el}} \left[\underbrace{\left(\tau_{supg} \left(\mathbf{u}^h \cdot \nabla \right) \mathbf{w}^h, \mathcal{R}^h \right)_{\Omega,e}}_{\text{SUPG stabilization}} + \underbrace{\left(\tau_{pspg} \nabla q^h, \mathcal{R}^h \right)_{\Omega,e}}_{\text{PSPG stabilization}} \right] = 0 \tag{4}$$

where Eq. (1) is the Navier-Stokes equation, Eq. (2) is the continuity equation, Eq. (3) describes the constitutive stress-strain law for Newtonian fluids, and Eq. (4) desribes the complete, generalized variational form for the stabilized finite element method described here. In the equations summarised here, $\mathbf{u}, p$ denote the blood flow velocity and pressure, $\mathbf{w}, q$ denote the finite element method test functions, μ_f is the blood viscosity, ρ_f is the blood density, $\mathbf{g}$ denotes gravity, Ω indicates the overall computational domain encompassing the arterial network, Γ and its sub-scripts denote the various boundary faces of the computational domain, $\mathcal{R}^h$ denote the residual of the momentum equation, and finally $\tau_{supg/pspg}$ are stabilization factors for the SUPG stabilization (for convective flow) and PSPG stabilization (for pressure stability using equal order finite elements) terms respectively. A common pulsatile flow profile, originally derived from phase-contrast magnetic resonance (PC-MR) measurements, was imposed at the inlet of the model at the aortic root to drive the flow. The average volumetric inflow was kept consistent across all the models at 79 ml/s (4.8 l/min). At the outlet boundaries, the influences of the downstream vascular beds were incorporated by assigning resistance based boundary conditions (that is, $\mathbf{h}_{0D}$ in Eq. (4)), which specifies a pressure given a computed flow rate. Resistance values at each outlet were assigned based on assumed target flow distributions described in [25, 28]. Specifically for the present study, the target flow distribution fractions across the six cerebral arteries connected at the CoW were held the same for all the 24 patient-CoW combination. These steps, and additional numerical details, have been more extensively discussed in [28, 30].

2.4 Embolus transport

Emboli were assumed to be spherical particles, and their trajectory across the arterial pathway were computed using a one-way coupled scheme, which assumes that a particle is influenced by the flow, but not vice-versa, in the large arteries modeled here. The fluid-particle interaction was based on a custom modified form of the classical Maxey-Riley equation [27]. Our modifications entailed incorporating near-wall shear gradient driven lift forces, accounting for particle collisions with artery walls, and elastohydrodynamic lubrication effects near-wall. The final form of the resultant modified Maxey-Riley equation is summarized as follows:

$$m_p \frac{d\mathbf{v}_p}{dt} = \underbrace{\frac{1}{2} \rho_f C_D \left(\pi R_p^2 \right) \parallel \mathbf{u} - \mathbf{v}_p \parallel (\mathbf{u} - \mathbf{v}_p)}_{\text{drag force}} + \underbrace{C_{sl} \rho_f R_p^2 \frac{\sqrt{\mu_f}}{\sqrt{\rho_f \parallel \omega \parallel}} \left[(\mathbf{u} - \mathbf{v}_p) \times \boldsymbol{\omega} \right]}_{\text{lift force (shear-gradient)}} + \underbrace{\mathcal{V}_p \left(-\nabla p + \nabla \cdot \boldsymbol{\tau} \right)}_{\text{fluid stresses, undisturbed flow}}$$
$$+ \underbrace{C_{am} \frac{\rho_f \mathcal{V}_p}{2} \left[\frac{D\mathbf{u}}{Dt} - \frac{d\mathbf{v}_p}{dt} \right]}_{\text{added mass}} + \underbrace{\left(m_p - \rho_f \mathcal{V}_p \right) \mathbf{g}}_{\text{buoyancy}} + \underbrace{\mathcal{I}(\mathcal{P}, \mathcal{W}) \left[\Delta \mathbf{v}_p (e_{lub}) \right]}_{\text{elastohydrodynamic wall-collisions}} , \tag{5}$$

where m_p denotes the mass of the particle (embolus), $\mathcal{V}_p$ is the particle volume, $\mathbf{v}_p$ is the particle translational velocity, and R_p is the particle radius. The terms C_D and C_{sl} denote the drag and shear-gradient lift force coefficients, computed using expressions described in [30]. Similarly, C_{am} denotes the added-mass coefficient, which is unity for spherical immersed bodies. The term $\omega = \nabla \times \mathbf{u}$ denote the flow vorticity at the location of the particle. Lastly, the function $\mathcal{I}(\mathcal{P}, \mathcal{W})$ is an indicator function, assuming a value of 1 if the embolus

particle $\mathcal{P}$ contacts the vessel wall $\mathcal{W}$, and a value of 0 otherwise. The term $[\Delta \mathbf{v}_p\,(e_{lub})]$ represents the contribution to momentum change induced by elastohydrodynamic lubrication and particle-wall collisions, modeled using a lubrication dependent restitution coefficient e_{lub}. The respective mathematical expressions and algorithmic issues for each of these terms have been described in more detail in [30, 28, 29]. Each individual particle (embolus) trajectory was integrated in time using an explicit Euler time integration scheme with a time-step of 0.1 ms.

2.5 Sampling based statistical framework

The combined fluid-particle scheme was embedded within a Monte Carlo sampling based framework, developed in [28], which is briefly described here. A multi-parameter design of experiments was devised, by considering two different embolus material compositions (labelled as $\mathcal{E}$), and (for each material) three different embolus sizes (labeled as $\mathcal{D}$). Ensembles of spherical emboli were then generated at various locations along the aorta inlet face, representing cardiogenic emboli entering the aortic arch. Each ensemble was generated to comprise approximately 4,020 particles. Eight characteristic release instances were chosen across the cardiac cycle (labeled as $\mathcal{T}$), where the embolus samples were released into the flow, and their trajectories integrated. The overall list of parametric combinations have been listed in Table 1. For each parametric combination, particle distribution to each vessel outlet was computed over 10 cardiac cycles, leading to a number fraction (by dividing by the ensemble size). Following the notation described in [28], the number fraction for the k'th vessel is defined as $\phi_k(\Lambda) = N_k/N_s$, where N_k is the number of embolic particles reaching the vessel k, N_s is the total number of particles in the ensemble, and Λ denotes the input vector comprising a combination of the various parameters defined herein i.e. $\Lambda_i = [\mathcal{D}_i, \mathcal{E}_i, \mathcal{T}_i; \mathcal{A}_i]$ where the factor $\mathcal{A}$ is a place-holder for the model anatomy of the CoW (Table 1). We further processed these number fractions ϕ_k to account for combined effect of underlying variables as well as to denote collections of vessels. For example, ϕ_{cow} will denote the total number fraction reaching the CoW, ϕ_{cow}^X will denote summation of number fractions across all variable combinations for the X'th variable. For the purpose of the present study, a variable of specific interest is the ratio $\overline{\phi_k} = \phi_k/\phi_{cow}$ for each of the six cerebral arteries, which denotes the proportion of cerebral emboli reaching the k'th cerebral artery, and sums to a total of 1.0 across all the six cerebral arteries.

2.6 Flow and embolus routing through Circle of Willis

A detailed post-processing protocol was devised to further analyze the influence of communicating arteries in routing particles, across the CoW anatomical variants considered. The steps of this procedure have been schematically outlined in Figure 2. First, the seven communicating arteries from the complete CoW anatomy were computationally isolated (Figure 2, step a.). Thereafter, the geometries of the extracted segments were processed, their centerlines were extracted, and a set of cross-sectional slices were created normal to the centerline along the length of each of the vessel segments - as described in Figure 2, step b. Following this, the blood flow velocity fields were interpolated at the locations of these section-planes, and the flow field as well as the volumetric flow rate carried by the communicating vessels were computed (Figure 2, step c.). Finally, a numeric index for the proportion of cerebral emboli carried by the specific communicating vessel segment was computed. This was achieved by choosing the midpoint of the centerline of each communicating vessel as a reference point, and identifying points along each embolic particle pathline that lie closest to this point. Each embolus trajectory was assigned a scalar value equal to the distance between these two points, and the trajectories were identified into clusters based on this distance. The smallest coherent cluster size was used as a metric for the total number of emboli carried by the communicating vessel segment in question (the trajectories marked in blue in Figure 2, step d.). This quantity has hereafter been referred to as routing count, and denoted by R_k for various communicating artery segments indexed by k. We remark that a simple counting of particles across the communicating segments would not be sufficient, since: (a) each particle can potentially travel across several vessel segments as they traverse the circle and exit into one of the six cerebral vascular beds, and (b) particles can often reverse their trajectories under retrograde/swirling flow.

3 Results

3.1 Circle of Willis anatomy influences embolus distribution

A key objective here is to establish whether the CoW anatomy has a significant, and quantifiable, influence on embolus distribution in the brain. We addressed this by computing variabilities induced in embolus distribution to cerebral arteries with respect to CoW anatomy, over and above any variabilities expected from flow distribution alone. For this, we computed the distribution ratio $\overline{\phi}_k^{\mathcal{T}}$ as defined in Section 2.5, for the left and right ACA, MCA, and PCA respectively. For each embolus composition and size, we compared this ratio across all the CoW anatomical variants. For each patient, we then computed the sample mean and standard deviation of these distribution ratios. A relative measure of variability in embolus distribution fractions for each cerebral artery was obtained by computing the coefficient of variation (cov_e) - defined as the ratio between the standard deviation and the mean of the distribution fraction data. Additionally we computed the corresponding mean, standard deviation, and coefficient of variation (cov_f) for the flow distribution ratios to each cerebral artery, for varying CoW anatomies. Dividing the cov_e by the corresponding cov_f values ensures that the scatter in embolus distribution is normalized against any existing variability induced by the flow distribution.

The ratio between the computed cov_e and cov_f has been compiled for thrombo-emboli and calcified-emboli of varying sizes in Table 2 and Table 3 respectively. The sample statistics of these $cov_e : cov_f$ ratios, for each cerebral artery, has been illustrated in Figure 3. If this ratio is equal to unity, variabilities in embolus and flow distribution are equivalent, while values greater than unity suggest embolus distribution manifests greater variability as compared to flow. We observe from Tables 2 and 3 that a significant number of these evaluated ratios deviate from unity. This is also evident from Figure 3 where a value of 1.0 is marked using a green solid line, and a significant number of samples lie above the line. Observing from Figure 3 that the sample distribution for the $cov_e : cov_f$ ratios is non-Gaussian, we employed a non-parametric Wilcoxon test for establishing how significantly these ratios differ from unity. Corresponding p-values were < 0.001 for left and right ACA, left and right PCA, and left MCA, and was 0.02 for the right MCA. This particular case of the MCA is further discussed in the next section. These observations indicate that scatter in embolus distribution is substantially different from what we would expect had flow distribution variabilities alone influenced it. Following the description of the parameter combinations as per Section 2.5, we observe that for each computed cov_e value, embolus properties were held fixed, and release times were summed over, leaving, for each patient, the CoW anatomy as the lone variable. Hence, the observed variabilities in embolus distribution here for each embolus type and size, can be attributed to the influence of anatomical variations.

3.2 Embolus distribution to MCA territory is least sensitive to Circle anatomy

Differences in embolus distribution induced due to variations in CoW anatomy are observed to vary notably across the six major cerebral arteries. In particular, from Tables 2 and 3, and Figure 3, it is seen that the embolus distribution *cov* values, and their ratios with respect to *cov* for flow, for both thrombo-emboli and calcified emboli are the lowest for the right and left MCA, across all embolus sizes and anatomical variants of the CoW. This indicates that the overall cardiogenic embolus distribution to the MCA territory is least sensitive to potential variabilities induced due to anatomical variations in the CoW. Figure 3 also indicates that, for the various cases considered here, the variability in cardiogenic embolus distribution to the right brain is noticeably lesser when compared with that for the left brain. The left and right MCA are usually the bigger vessels amongst the six cerebral arteries, carrying a greater proportion of blood into the brain. Additionally, anatomically the MCAs have a greater tendency to receive emboli directly traversing the ICAs. As inertial embolic particles enter the aorta from the heart, they follow the greater curvature of the aortic arch, where they encounter the right branching vessels first, and follow on into the right carotid artery. These factors together explain the lower sensitivity of middle brain embolus distribution, and stronger right brain preference, as observed here. The prominent right-brain and middle-brain propensity of cardiogenic emboli have been reported in our prior studies [28] as well as clinical studies [18, 31], indicating that the reported trends here are consistent.

3.3 Circle of Willis anatomy potentially impacts proximal cervical flow

The developed simulation framework incorporates the entire network of major supplying arteries from the heart to the CoW. This has the benefit of enabling investigations on correlations between flow at the cerebral arteries and at other locations upstream. In particular, here we computed the flow through the ICAs and BA (i.e. total flow through the proximal cervical vessels), and compared them across the various patients and CoW anatomies considered. Figure 4 illustrates the ratio between flow through L.ICA and BA (top), between R.ICA and BA (middle), and between right and left ICAs (bottom) for all the patients considered in our study. We observe from these results that anatomical variations of the CoW has a notable influence on the proportion of flow across the ICAs and BA, as well as on left-right asymmetry in flow through the ICAs. While the absence of the AcoA, L.Comm, and R.Comm segments are seen to induce small but noticeable changes in the relative flow through the ICAs and BA, the most significant influence is observed for the cases with missing LP1 and RP1 segments (fetal-type CoW anatomy). The results in Figure 4 indicate that absence of LP1 connector segment causes a significant increase in flow through left ICA with respect to BA, as well as reduces the right vs left asymmetry in ICA flow (and vice-versa for the absence of RP1 connector segment). The results collectively indicate that in all cases, the fetal type variants lead to increased ipsilateral flow through the ICAs. The aforementioned trends with respect to the fetal-type CoW anatomy variants can be explained as a consequence of ICA flow trying to compensate for the deficit in PCA flow due to the BA not directly supplying the posterior cerebral vasculature. We note that these simulation results are based on the underlying assumption that the cerebral beds fed by the six major cerebral arteries maintain the same flow requirements across the various CoW anatomical variants. However, the findings are in agreement with previous clinical studies [37], and indicate that CoW anatomy may manifest itself in how flow through the cervical vasculature reaches the brain.

3.4 Communicating arteries and their role in flow routing

As blood flow enters the CoW via the left and right ICA and BA, and redistributes to meet the flow demands at each of the six major cerebral vascular regions, the communicating arteries of the CoW play a key role in determining the proximal collateral capability of cerebral vasculature. The differential routing of flow across these artery segments, for various CoW anatomy variants, potentially enables a mechanistic reasoning for the influence of CoW anatomy on embolus distribution. To characterize this, we used the method in Section 2.6 to estimate the volumetric flow across each communicating artery segment for all the 24 patient-CoW combinations. The results have been illustrated in Figures 5 and 6. Figure 5 compares the volumetric flow rate at peak systole across each of the seven communicating artery segments. For each patient, it is observed that CoW anatomical variations lead to noticeable differences in the extent of flow being routed across the communicating arteries. Further details are illustrated in Figure 6, which depicts the time-averaged volumetric flow-rate (across one cardiac cycle) across each communicating artery for the full CoW anatomy (the first column), and compares the factor by which the flow changes, as well as the flow direction, for all the remaining corresponding anatomical variations. All flow rates presented are in units of ml/min. It is observed that the CoW anatomy variants can alter not only the amount of flow routed across the communicating vessels, but also the direction in which flow is carried along the CoW. When we compare the factors by which flow carried by the communicating vessels change, it is observed that the L.Comm, R.Comm, and AcoA segments show notably greater variability in their flow engagement compared to all other communicating segments. On the other hand, the LP1 and RP1 segments show the least variability in their flow engagement. Additionally, the anatomy variants with missing LP1/RP1 segments are seen to have the most prominent differences in flow routed across the CoW. For these anatomies, the L.Comm and R.Comm segments are seen to be extensively engaged, and play a key role in distributing flow. This is in contrast with all the other anastomoses where the proportion of flow carried by the L.Comm and R.Comm segments are quite low when compared to the left and right P1 and A1 connector segments. Our observations also indicate that the AcoA can carry significant extent of flow, sometimes even reversing the direction of flow, to maintain a left-right proximal collateral pathway for blood flow distribution in the brain. This quantitative evidence for the role of AcoA in the proximal collateral capacity of the CoW, is in agreement with observations from clinical studies on collateral flow characteristics of the brain [19, 14, 41]. Furthermore, the general computational observations on CoW communicating arteries actively engaging in flow routing is in reasonable agreement with observations from clinical data [13].

3.5 Embolus transport across communicating arteries

Blood flow is differentially routed across the CoW for varying anatomy. While hemodynamic forces drive the dynamics of embolic particles traversing the arterial network, actual embolus trajectories will not exactly follow the differences in flow across the communicating arteries, owing to their finite inertia (leading to a finite response time for emboli to be influenced by forces due to the flow) and changes in trajectory due to collisions with the vessel wall. Hence, to complete the mechanistic reasoning for the influence of CoW anatomy on embolus distribution, we further quantify the embolus routing statistics, using the routing count variable R_k (as defined in Section 2.6) for six communicating artery segments (indexed by k) - L.Comm, R.Comm, LA1, RA1, LP1, and RP1. Owing to the complexity and tortuosity of the anatomy at the location of the AcoA, it was not possible to get a clear definition of R_k for this segment. The resultant routing count for each of the six communicating vessel segments were compiled for all possible parameter combinations employed in this study, and post-processed to illustrate the trends in embolic particle transport across the CoW. First, R_k values for each communicating segment in the incomplete CoW anatomies were compared with the corresponding values for the segments in the complete CoW. Sample distribution of these ratios have been illustrated in Figure 7.a. A value of unity would indicate that the number of emboli traversing a vessel did not change with CoW anatomy. The observed ratios in Figure 7.a. are notably different from unity, indicating thereby that the resultant embolus trajectories, en-route to exiting one of the six major cerebral arteries, are significantly influenced by the CoW anatomy variations. The relative importance of each communicating vessel segment in transporting emboli is illustrated in Figure 7.b., where R_k values for each of the vessels within a particular CoW anatomy have been normalized with respect to the maximum R_k observed for that geometry. Thus values closer to unity in Figure 7.b. indicate a high extent of embolus traversal across the vessel segment and vice-versa. It is observed that the LA1 and RA1 segments are associated with the greatest extent of embolus traversal, and the L.Comm and R.Comm segments are associated with the least extent of embolus traversal. Furthermore, the influence of the individual embolus properties (size, and material composition) have been isolated and illustrated in Figure. 7.c. and Figure 7.d. These panels, depict the maximum, and the total R_k values across all the different communicating vessels respectively, and a high value along the y-axis denotes a large number of emboli that actually were routed across these vessels, while a low value indicates minimal engagement of these vessels in distributing emboli to the distal cerebral vasculature beds. The results indicate a strong influence of the embolus particle inertia, as well as density ratio between embolus and blood, in governing their re-routing across the CoW - with the general trend being that larger and denser emboli tend to enter and exit the CoW with less traversal across the communicating vessels.

4 Discussion

4.1 Cerebral vasculature and cardio-embolic stroke

Our simulations illustrate the routing of flow across the CoW artery segments for varying anatomy, and indicate that interaction of inertial embolic particles with re-routed flow leads to differences in embolus distribution to the major cerebral vascular beds. Consequently, cerebral vasculature can be thought to play a bipartite role in ischemic events. The first, and better known, role is in terms of flow compensation during occlusion, and collateral circulation. The second role, as demonstrated here, comprises the cerebral vasculature influencing embolus transport leading to potential ischemia. Mechanistically, emboli entering the CoW from a supplying vessel (e.g. ICA) may not actually exit into the immediately connected cerebral artery (e.g. MCA) as expected from anatomical considerations alone, but instead traverse several vessel segments to exit at another location. These insights on the role of cerebral vasculature on embolic stroke obtained from our study are critical for evaluating the source of emboli [36]. Thus, our model would allow clinicians to direct therapy (surgical, interventional or pharmacologic) to the appropriate anatomy in patients with multiple potential sources of emboli. Resolving sources of emboli are particularly important in patient with ambiguous clinical history such as moderate diffuse atherosclerosis with a hypoperfusive event. Also of clinical relevance are cases of artery to artery microemboli in intracranial atherosclerosis or other arterial disease [39, 11]. Our data suggest that these microemboli trajectories are more influenced by COW anatomy and thus may generate non-intuitive locations for distal infarction.

4.2 The triad of anatomy, flow, and embolus properties

The biomechanical events governing embolus transport to the brain (or other key organs) comprise a synergistic interplay of three factors: anatomical features, hemodynamics, and embolus properties. Anatomical features like curvature and tortuosity of vessels, vessel segment interconnectivity, and branching has a strong influence on the three-dimensional flow patterns through these vessels. Notably, pulsatile viscous flow through such realistic anatomical vasculature is associated with extensive vorticity, swirling flow, and retrograde flow during the deceleration phase of the cardiac cycle. Embolus particles of finite size and inertia interact with these spatio-temporally varying flow structures, leading to a nearly chaotic advection from their origin site to their destination [30]. It can be shown from a mathematical analysis of the underlying equations governing embolus dynamics that two key non-dimensional variables govern their motion [29]. First, the momentum response time (referred often by the related non-dimensional Stokes number) governs how quickly the particle responds to the forces from the blood flow. Second, the density ratio between the embolus and blood, which governs how buoyant the embolus is within the vessel. This is clearly observed in Figures 7.c. and 7.d., where the two dashed lines represent constant density-ratios, and variations along each represent how momentum response time influences R_k. In prior work, we have isolated the influence of these three factors in the context of anatomy of the aortic arch, determining whether emboli are routed towards or away from the brain. The results from this study illustrates the same influence in the context of the anatomy of the CoW, which determines which of the six major cerebral vasculature beds does an incoming emboli go to.

4.3 Assumptions and limitations

The underlying computational modeling framework was based on few key assumptions. Firstly, as discussed in our prior works, the influence of the embolus particle on the blood flow was not accounted for, leading to a one-way interaction between the flow and emboli. Hence, our study focused on emboli sizes that are in the small-to-medium regime with respect to the vessel sizes, such that potential occlusions in vasculature beds at or proximal to the M1, A1, and P1 segments are not considered. While a fully-resolved coupling is mathematically more accurate, it is also significantly expensive, which would render the kind of sampling based analysis presented here untenable. The one-way interaction model used here has been validated previously for both industrial and cardiovascular applications, with our prior works demonstrating that this approach is reasonable for the small-to-medium size ratios considered here [29]. Further in-depth investigations on fully resolved two-way fluid particle interactions for complex cardiovascular flows is an area that needs separate investigation by itself, and comprises a parallel focus of our current research interests. Secondly, it was assumed that the removal of one communicating vessel segment from the CoW would not influence the size and length of the remaining communicating segments. This was primarily because well characterized human population data on this was not available, and introducing arbitrary geometric rules to model any vessel size changes was avoided in our framework. However, the image-based modeling step in our framework is flexible as it deals with individual vessels at the level of segmentations, and any trends in vessel shape with respect to CoW topology can be easily incorporated. Thirdly, the influence of dynamic cerebral autoregulation has not been included within the model. While this may certainly alter the model predictions for embolus transport in patients who have already had a stroke or a transient ischemic attack, this was not a factor for our study as we considered healthy patients, and were looking at the event horizon prior to any cerebro-embolic event. Finally, a key study limitation was the small population size considered here. While we considered four different patients, with six different CoW topological variants, this was still a smaller subject cohort size, and renders some restrictions in terms of characterizing inter-patient variabilities and patient statistics. The findings presented here, however, still retain their significance in terms of providing numerical evidence on the role of CoW anatomy in embolus transport and embolic stroke risk, and the corresponding hemodynamic connection.

4.4 Broader implications

The computer simulation framework, and the data, described here have broader implications in terms of stroke diagnosis and treatment. The approach can complement current clinical imaging protocols in helping make patient-specific predictions on embolic risks by integrating CT/MR/Trans-cranial Doppler data with numerical modeling of various embolism scenarios as described here. This can be used to disambiguate the

source of emboli in patients with multiple sources. In addition, our results show that likelihood of cardio-embolic sources being responsible for specific infarct patterns is composed of both general patterns and patient specific patterns. One notable general pattern is the right MCA territory being least variable in its likelihood of emboli. It remains intriguing that our data suggest a protective effect for the left hemisphere vis a vis embolic material; indicating that anatomy and physiology apparently recognize the importance of language dominance and the devastating effects of left MCA stroke. Furthermore, insertion of catheters or other endovascular devices commonly employed in surgical treatments, can effectively alter blood flow in similar ways as hypoplasia/aplasia of communicating arteries in the CoW [24]. Thus, collateral capacity through the communicating arteries of the CoW influence ischemic risks during procedures like carotid endarterectomy [17]. The methodology developed here can help address effectiveness of cerebral vasculature in maintaining perfusion during a procedure, and evaluating peri-operative embolic stroke risks due to emboli released during a procedure due to endothelial trauma [1], or plaque rupture. Finally, the influence of the CoW anatomy on flow re-distribution, and particle routing, is also of importance for drug delivery techniques in the brain. For example, shear activated particle based drugs for thrombolysis have shown great promise in recent investigations [20, 26]. The tools and findings described here could be of benefit in successfully transforming such techniques into more effective stroke treatment approaches.

5 Concluding Remarks

In this study we described a patient-specific simulation based study to investigate the role of the anatomy of the Circle of Willis (CoW) in embolic stroke. We performed systematic parametric experimentation on transport of cardiogenic emboli of varying sizes and compositions in four patient vasculature geometries, considering six different anatomical variants of the CoW. The resultant data and statistics helped establish that CoW anatomical variations do play a role in altering embolus distribution in the brain, and that middle brain embolism risks are least sensitive to this anatomical influence. The ability to extract fully resolved flow and embolus trajectory information also helped illustrate the mechanical phenomena that leads to these variations in embolus distribution. The findings indicated that anatomical variations lead to differences in flow routing from the internal carotid and basilar arteries, across the various communicating artery segments of the CoW, into the six major cerebral arteries. Embolic particles of finite size and inertia interact with the flow routed across the vessel segments, and traverse the CoW based on these interactions, leading to a difference in their final destination cerebral vasculature bed. The computatonal approach as well as the resulting findings have broad impacts on understanding stroke biomechanics, stroke diagnosis, and treatment planning.

6 Conflicts of Interest

There are no conflicts of interest.

7 Acknowledgements

This work was supported by the American Heart Association Award: 13GRNT17070095. This research used the Savio computational cluster resource provided by the Berkeley Research Computing program at the University of California, Berkeley. NDJ acknowledges support from the Regent's and Chancellor's Research Fellowship at U.C. Berkeley. DM, NDJ, and SCS conceptualized the design of the study. DM developed the computational framework, performed the embolus dynamics, performed all statistical and data analysis, drafted the manuscript. NDJ devised the image-based modeling framework, computed all flow simulations, and contributed to embolus dynamics simulations. JN helped with data analysis, and contributed clinical and diagnostic connections to the simulation data. NDJ, SCS, and JN reviewed and edited the manuscript draft. Final manuscript version was in agreement with all Authors.

References

[1] P.T. Akins, A.P. Amar, R.S. Pakbaz, and J.D. Fields. Complications of endovascular treatment for acute stroke in the swift trial with solitaire and merci devices. *American Journal of Neuroradiology*, 35(3):524–528, 2014.

[2] J. Alastruey, K.H. Parker, J. Peiró, S.M. Byrd, and S.J. Sherwin. Modelling the circle of willis to assess the effects of anatomical variations and occlusions on cerebral flows. *Journal of biomechanics*, 40(8):1794–1805, 2007.

[3] M.S. Alnæs, J. Isaksen, K.A. Mardal, B. Romner, M.K. Morgan, and T. Ingebrigtsen. Computation of hemodynamics in the circle of willis. *Stroke*, 38(9):2500–2505, 2007.

[4] B.J. Alpers and R.G. Berry. Circle of willis in cerebral vascular disorders: the anatomical structure. *Archives of Neurology*, 8(4):398–402, 1963.

[5] B.J. Alpers, R.G. Berry, and R.M. Paddison. Anatomical studies of the circle of willis in normal brain. *AMA Archives of Neurology & Psychiatry*, 81(4):409–418, 1959.

[6] A. Arboix and J. Alioc. Cardioembolic stroke: clinical features, specific cardiac disorders and prognosis. *Current cardiology reviews*, 6(3):150–161, 2010.

[7] I.A. Carr, N. Nemoto, R.S. Schwartz, and S.C. Shadden. Size-dependent predilections of cardiogenic embolic transport. *American Journal of Physiology-Heart and Circulatory Physiology*, 305(5):H732–H739, 2013.

[8] K. DeVault, P.A. Gremaud, V. Novak, M.S. Olufsen, G. Vernieres, and P. Zhao. Blood flow in the circle of willis: modeling and calibration. *Multiscale Modeling & Simulation*, 7(2):888–909, 2008.

[9] J.M. Ferro. Cardioembolic stroke: an update. *The lancet neurology*, 2(3):177–188, 2003.

[10] J.M. Ferro, A.R. Massaro, and J.L. Mas. Aetiological diagnosis of ischaemic stroke in young adults. *The Lancet Neurology*, 9(11):1085–1096, 2010.

[11] R.F. Gottesman, P.M. Sherman, M.A. Grega, D.M. Yousem, L.M. Borowicz, O.A. Selnes, W.A. Baumgartner, and G.M. McKhann. Watershed strokes after cardiac surgery. *Stroke*, 37(9):2306–2311, 2006.

[12] R.G. Hart, H.C. Diener, S.B. Coutts, J.D. Easton, C.B. Granger, M.J. O'Donnell, R.L. Sacco, S.J. Connolly, Cryptogenic Stroke/ESUS International Working Group, et al. Embolic strokes of undetermined source: the case for a new clinical construct. *The Lancet Neurology*, 13(4):429–438, 2014.

[13] A.W.J. Hoksbergen, B. Fülesdi, D.A. Legemate, and L. Csiba. Collateral configuration of the circle of willis. *Stroke*, 31(6):1346–1351, 2000.

[14] A.W.J. Hoksbergen, D.A. Legemate, L. Csiba, G. Csati, P. Siro, and B. Fülesdi. Absent collateral function of the circle of willis as risk factor for ischemic stroke. *Cerebrovascular Diseases*, 16(3):191–198, 2003.

[15] A.W.J. Hoksbergen, D.A. Legemate, D.T. Ubbink, and M.J.H.M. Jacobs. Collateral variations in circle of willis in atherosclerotic population assessed by means of transcranial color-coded duplex ultrasonography. *Stroke*, 31(7):1656–1660, 2000.

[16] K. Kapoor, B. Singh, and Late I.J. Dewan. Variations in the configuration of the circle of willis. *Anatomical science international*, 83(2):96–106, 2008.

[17] G.E. Kim, Y.P. Cho, and S.M. Lim. The anatomy of the circle of willis as a predictive factor for intra-operative cerebral ischemia (shunt need) during carotid endarterectomy. *Neurological research*, 24(3):237–240, 2002.

[18] H.J. Kim, J.M. Song, S.U. Kwon, B.J. Kim, D.H. Kang, J.K. Song, J.S. Kim, and D.W. Kang. Right–left propensity and lesion patterns between cardiogenic and aortogenic cerebral embolisms. *Stroke*, 42(8):2323–2325, 2011.

[19] M Kluytmans, J Van der Grond, K.J. Van Everdingen, C.J.M. Klijn, L.J. Kappelle, and M.A. Viergever. Cerebral hemodynamics in relation to patterns of collateral flow. *Stroke*, 30(7):1432–1439, 1999.

[20] N. Korin, M. Kanapathipillai, B.D. Matthews, M. Crescente, A. Brill, T. Mammoto, K. Ghosh, S. Jurek, S.A. Bencherif, D. Bhatta, et al. Shear-activated nanotherapeutics for drug targeting to obstructed blood vessels. *Science*, 337(6095):738–742, 2012.

[21] A. Krishnaswamy, J.P. Klein, and S.R. Kapadia. Clinical cerebrovascular anatomy. *Catheterization and Cardiovascular Interventions*, 75(4):530–539, 2010.

[22] A.S. Les, S.C. Shadden, C.A. Figueroa, J.M. Park, M.M. Tedesco, R.J. Herfkens, R.L. Dalman, and C.A. Taylor. Quantification of hemodynamics in abdominal aortic aneurysms during rest and exercise using magnetic resonance imaging and computational fluid dynamics. *Annals of Biomedical Engineering*, 38(4):1288–1313, 2010.

[23] D.S. Liebeskind. Collateral circulation. *Stroke*, 34(9):2279–2284, 2003.

[24] B. Lubicz, L. Collignon, G. Raphaeli, J.P. Pruvo, M. Bruneau, O. De Witte, and X. Leclerc. Flow-diverter stent for the endovascular treatment of intracranial aneurysms. *Stroke*, 41(10):2247–2253, 2010.

[25] M.E. MacDonald and R. Frayne. Phase contrast MR imaging measurements of blood flow in healthy human cerebral vessel segments. *Physiological Measurement*, 36(7):1517–1527, 2015.

[26] M.G. Marosfoi, N. Korin, M.J. Gounis, O. Uzun, S. Vedantham, E.T. Langan, A.L. Papa, O.W. Brooks, C. Johnson, A.S. Puri, et al. Shear-activated nanoparticle aggregates combined with temporary endovascular bypass to treat large vessel occlusion. *Stroke*, 46(12):3507–3513, 2015.

[27] M.R. Maxey and J.J. Riley. Equation of motion for a small rigid sphere in a nonuniform flow. *The Physics of Fluids*, 26(4):883–889, 1983.

[28] D. Mukherjee, N.D. Jani, K. Selvaganesan, C.L. Weng, and S.C. Shadden. Computational assessment of the relation between embolism source and embolus distribution to the circle of willis for improved understanding of stroke etiology. *Journal of Biomechanical Engineering*, 138(8):081008, 2016.

[29] D. Mukherjee, J. Padilla, and S.C. Shadden. Numerical investigation of fluid–particle interactions for embolic stroke. *Theoretical and Computational Fluid Dynamics*, 30(1-2):23–39, 2016.

[30] D. Mukherjee and S.C. Shadden. Inertial particle dynamics in large artery flows–implications for modeling arterial embolisms. *Journal of Biomechanics*, 52:155–164, 2017.

[31] N. Patel, M.A. Horsfield, C. Banahan, J. Janus, K. Masters, J. Morlese, V. Egan, and E.M.L. Chung. Impact of perioperative infarcts after cardiac surgery. *Stroke*, 46:680–686, 2015.

[32] E.B. Ringelstein, C. Weiller, M. Weckesser, and S. Weckesser. Cerebral vasomotor reactivity is significantly reduced in low-flow as compared to thromboembolic infarctions: the key role of the circle of willis. *Journal of the neurological sciences*, 121(1):103–109, 1994.

[33] D.F. Schomer, M.P. Marks, G.K. Steinberg, I.M. Johnstone, D.B. Boothroyd, M.R. Ross, N.J. Pelc, and D.R. Enzmann. The anatomy of the posterior communicating artery as a risk factor for ischemic cerebral infarction. *New England Journal of Medicine*, 330(22):1565–1570, 1994.

[34] W.S. Smith, M.H. Lev, J.D. English, E.C. Camargo, M. Chou, S.C. Johnston, G. Gonzalez, P.W. Schaefer, W.P. Dillon, W.J. Koroshetz, and K.L. Furie. Significance of large vessel intracranial occlusion causing acute ischemic stroke and tia. *Stroke*, 40(12):3834–3840, 2009.

[35] D.A. Steinman. Image-based computational fluid dynamics modeling in realistic arterial geometries. *Annals of biomedical engineering*, 30(4):483–497, 2002.

[36] K. Szabo, R. Kern, A. Gass, J. Hirsch, and M. Hennerici. Acute stroke patterns in patients with internal carotid artery disease. *Stroke*, 32(6):1323–1329, 2001.

[37] H. Tanaka, N. Fujita, T. Enoki, K. Matsumoto, Y. Watanabe, K. Murase, and H. Nakamura. Relationship between variations in the circle of willis and flow rates in internal carotid and basilar arteries determined by means of magnetic resonance imaging with semiautomated lumen segmentation: reference data from 125 healthy volunteers. *American journal of neuroradiology*, 27(8):1770–1775, 2006.

[38] C.A. Taylor and D.A. Steinman. Image-based modeling of blood flow and vessel wall dynamics: applications, methods and future directions. *Annals of biomedical engineering*, 38(3):1188–1203, 2010.

[39] A. Torvik. The pathogenesis of watershed infarcts in the brain. *Stroke*, 15(2):221–223, 1984.

[40] A. Updegrove, N.M. Wilson, J. Merkow, H. Lan, A.L. Marsden, and S.C. Shadden. Simvascular: An open source pipeline for cardiovascular simulation. *Annals of Biomedical Engineering*, pages 1–17, 2016.

[41] T. van Seeters, J. Hendrikse, G.J. Biessels, B.K. Velthuis, W.P.T.M. Mali, L.J. Kappelle, Y. van der Graaf, SMART Study Group, et al. Completeness of the circle of willis and risk of ischemic stroke in patients without cerebrovascular disease. *Neuroradiology*, 57(12):1247–1251, 2015.

Figures And Tables

Table 1: *Table outlining the various parameter combinations incorporated in the simulation study presented here. The full set of numerical experiments presented here spans a total of 1152 parameter combinations, with around 4,020 virtual embolus particles tracked per combination.*

Patient: $\{\mathcal{P}_1, \mathcal{P}_2, \mathcal{P}_3, \mathcal{P}_4\}$	$\mathcal{A}_1$: full CoW	$\mathcal{E}_1$: thrombo-emboli	$\mathcal{D}_1$: 100 μm	$\mathcal{T} = \{\mathcal{T}_i; i = 1, \cdots, 8\}$
			$\mathcal{D}_2$: 500 μm	$\mathcal{T} = \{\mathcal{T}_i; i = 1, \cdots, 8\}$
			$\mathcal{D}_3$: 1000 μm	$\mathcal{T} = \{\mathcal{T}_i; i = 1, \cdots, 8\}$
		$\mathcal{E}_2$: calcific-emboli	$\mathcal{D}_1$: 100 μm	$\mathcal{T} = \{\mathcal{T}_i; i = 1, \cdots, 8\}$
			$\mathcal{D}_2$: 500 μm	$\mathcal{T} = \{\mathcal{T}_i; i = 1, \cdots, 8\}$
			$\mathcal{D}_3$: 1000 μm	$\mathcal{T} = \{\mathcal{T}_i; i = 1, \cdots, 8\}$
	$\mathcal{A}_2$: no AcoA	$\mathcal{E}_1$: thrombo-emboli	$\mathcal{D}_1$: 100 μm	$\mathcal{T} = \{\mathcal{T}_i; i = 1, \cdots, 8\}$
			$\mathcal{D}_2$: 500 μm	$\mathcal{T} = \{\mathcal{T}_i; i = 1, \cdots, 8\}$
			$\mathcal{D}_3$: 1000 μm	$\mathcal{T} = \{\mathcal{T}_i; i = 1, \cdots, 8\}$
		$\mathcal{E}_2$: calcific-emboli	$\mathcal{D}_1$: 100 μm	$\mathcal{T} = \{\mathcal{T}_i; i = 1, \cdots, 8\}$
			$\mathcal{D}_2$: 500 μm	$\mathcal{T} = \{\mathcal{T}_i; i = 1, \cdots, 8\}$
			$\mathcal{D}_3$: 1000 μm	$\mathcal{T} = \{\mathcal{T}_i; i = 1, \cdots, 8\}$
	$\mathcal{A}_3$: no LComm	$\mathcal{E}_1$: thrombo-emboli	$\mathcal{D}_1$: 100 μm	$\mathcal{T} = \{\mathcal{T}_i; i = 1, \cdots, 8\}$
			$\mathcal{D}_2$: 500 μm	$\mathcal{T} = \{\mathcal{T}_i; i = 1, \cdots, 8\}$
			$\mathcal{D}_3$: 1000 μm	$\mathcal{T} = \{\mathcal{T}_i; i = 1, \cdots, 8\}$
		$\mathcal{E}_2$: calcific-emboli	$\mathcal{D}_1$: 100 μm	$\mathcal{T} = \{\mathcal{T}_i; i = 1, \cdots, 8\}$
			$\mathcal{D}_2$: 500 μm	$\mathcal{T} = \{\mathcal{T}_i; i = 1, \cdots, 8\}$
			$\mathcal{D}_3$: 1000 μm	$\mathcal{T} = \{\mathcal{T}_i; i = 1, \cdots, 8\}$
	$\mathcal{A}_4$: no LP1	$\mathcal{E}_1$: thrombo-emboli	$\mathcal{D}_1$: 100 μm	$\mathcal{T} = \{\mathcal{T}_i; i = 1, \cdots, 8\}$
			$\mathcal{D}_2$: 500 μm	$\mathcal{T} = \{\mathcal{T}_i; i = 1, \cdots, 8\}$
			$\mathcal{D}_3$: 1000 μm	$\mathcal{T} = \{\mathcal{T}_i; i = 1, \cdots, 8\}$
		$\mathcal{E}_2$: calcific-emboli	$\mathcal{D}_1$: 100 μm	$\mathcal{T} = \{\mathcal{T}_i; i = 1, \cdots, 8\}$
			$\mathcal{D}_2$: 500 μm	$\mathcal{T} = \{\mathcal{T}_i; i = 1, \cdots, 8\}$
			$\mathcal{D}_3$: 1000 μm	$\mathcal{T} = \{\mathcal{T}_i; i = 1, \cdots, 8\}$
	$\mathcal{A}_5$: no RComm	$\mathcal{E}_1$: thrombo-emboli	$\mathcal{D}_1$: 100 μm	$\mathcal{T} = \{\mathcal{T}_i; i = 1, \cdots, 8\}$
			$\mathcal{D}_2$: 500 μm	$\mathcal{T} = \{\mathcal{T}_i; i = 1, \cdots, 8\}$
			$\mathcal{D}_3$: 1000 μm	$\mathcal{T} = \{\mathcal{T}_i; i = 1, \cdots, 8\}$
		$\mathcal{E}_2$: calcific-emboli	$\mathcal{D}_1$: 100 μm	$\mathcal{T} = \{\mathcal{T}_i; i = 1, \cdots, 8\}$
			$\mathcal{D}_2$: 500 μm	$\mathcal{T} = \{\mathcal{T}_i; i = 1, \cdots, 8\}$
			$\mathcal{D}_3$: 1000 μm	$\mathcal{T} = \{\mathcal{T}_i; i = 1, \cdots, 8\}$
	$\mathcal{A}_6$: no RP1	$\mathcal{E}_1$: thrombo-emboli	$\mathcal{D}_1$: 100 μm	$\mathcal{T} = \{\mathcal{T}_i; i = 1, \cdots, 8\}$
			$\mathcal{D}_2$: 500 μm	$\mathcal{T} = \{\mathcal{T}_i; i = 1, \cdots, 8\}$
			$\mathcal{D}_3$: 1000 μm	$\mathcal{T} = \{\mathcal{T}_i; i = 1, \cdots, 8\}$
		$\mathcal{E}_2$: calcific-emboli	$\mathcal{D}_1$: 100 μm	$\mathcal{T} = \{\mathcal{T}_i; i = 1, \cdots, 8\}$
			$\mathcal{D}_2$: 500 μm	$\mathcal{T} = \{\mathcal{T}_i; i = 1, \cdots, 8\}$
			$\mathcal{D}_3$: 1000 μm	$\mathcal{T} = \{\mathcal{T}_i; i = 1, \cdots, 8\}$

Table 2: *Simulation data for coefficients of variation of thrombo-emboli distribution to the six major cerebral arteries across all anatomical variations considered, and the ratio between embolus and flow coefficients of variation. Varying embolus sizes denoted by* $\mathcal{D}_{1/2/3}$.

Cases		Cerebral arteries					
Patient	Size	LACA	LMCA	LPCA	RACA	RMCA	RPCA
Patient: $\mathcal{P}_1$	Ratio of $(c.o.v)_e$ w.r.t. $(c.o.v)_f$						
	$\mathcal{D}_1$	2.59	0.76	2.95	3.42	0.85	1.55
	$\mathcal{D}_2$	1.04	0.58	5.11	6.02	0.55	2.43
	$\mathcal{D}_3$	4.02	1.03	6.08	7.98	1.43	2.93
	Sample coefficients of variation						
	$\mathcal{D}_1$	0.0798	0.0761	0.0723	0.0713	0.0810	0.0964
	$\mathcal{D}_2$	0.0320	0.0584	0.1251	0.1254	0.0530	0.1513
	$\mathcal{D}_3$	0.1241	0.1032	0.1488	0.1662	0.1366	0.1824
	flow	0.0309	0.1006	0.0245	0.0208	0.0956	0.0622
Patient: $\mathcal{P}_2$	Ratio of $(c.o.v)_e$ w.r.t. $(c.o.v)_f$						
	$\mathcal{D}_1$	6.07	1.16	1.03	1.95	0.90	1.20
	$\mathcal{D}_2$	7.46	1.10	1.97	2.63	0.51	1.41
	$\mathcal{D}_3$	43.16	2.39	4.30	8.70	0.91	3.33
	Sample coefficients of variation						
	$\mathcal{D}_1$	0.1333	0.1744	0.2013	0.2106	0.2036	0.2613
	$\mathcal{D}_2$	0.1637	0.1663	0.3833	0.2845	0.1159	0.3065
	$\mathcal{D}_3$	0.9470	0.3597	0.8374	0.9394	0.2056	0.7256
	flow	0.0219	0.1506	0.1947	0.1080	0.2255	0.2180
Patient: $\mathcal{P}_3$	Ratio of $(c.o.v)_e$ w.r.t. $(c.o.v)_f$						
	$\mathcal{D}_1$	1.10	1.05	1.84	0.96	0.90	0.99
	$\mathcal{D}_2$	1.50	1.70	2.67	0.76	0.79	1.23
	$\mathcal{D}_3$	3.65	4.03	7.34	1.83	1.08	1.30
	Sample coefficients of variation						
	$\mathcal{D}_1$	0.1786	0.0876	0.1437	0.1614	0.1673	0.1785
	$\mathcal{D}_2$	0.2437	0.1416	0.2088	0.1282	0.1479	0.2218
	$\mathcal{D}_3$	0.5922	0.3364	0.5734	0.3080	0.2009	0.2348
	flow	0.1621	0.0835	0.0782	0.1680	0.1869	0.1808
Patient: $\mathcal{P}_4$	Ratio of $(c.o.v)_e$ w.r.t. $(c.o.v)_f$						
	$\mathcal{D}_1$	5.97	2.21	2.94	5.47	4.27	2.34
	$\mathcal{D}_2$	5.91	2.52	4.28	12.80	3.75	2.23
	$\mathcal{D}_3$	47.31	2.13	18.75	18.93	4.36	3.50
	Sample coefficients of variation						
	$\mathcal{D}_1$	0.0842	0.0421	0.0945	0.0545	0.0913	0.1059
	$\mathcal{D}_2$	0.0833	0.0481	0.1377	0.1275	0.0801	0.1011
	$\mathcal{D}_3$	0.6668	0.0406	0.6036	0.1885	0.0932	0.1584
	flow	0.0141	0.0191	0.0322	0.0100	0.0214	0.0452

Table 3: *Simulation data for coefficients of variation of thrombo-emboli distribution to the six major cerebral arteries across all anatomical variations considered, and the ratio between embolus and flow coefficients of variation. Varying embolus sizes denoted by $\mathcal{D}_{1/2/3}$. Note that for patients 1 & 4 largest calcified embolic fragments are too heavy to reach the brain at all.*

Cases		Cerebral arteries					
Patient	Size	LACA	LMCA	LPCA	RACA	RMCA	RPCA
Patient: $\mathcal{P}_1$	Ratio of $(c.o.v)_e$ w.r.t. $(c.o.v)_f$						
	$\mathcal{D}_1$	4.80	0.61	37.19	8.50	0.95	16.74
	$\mathcal{D}_2$	28.75	3.07	100.02	107.84	9.88	0.00
	$\mathcal{D}_3$	0.00	0.00	0.00	0.00	0.00	0.00
	Sample coefficients of variation						
	$\mathcal{D}_1$	0.1481	0.0616	0.9109	0.1771	0.0910	1.0414
	$\mathcal{D}_2$	0.8870	0.3088	2.4495	2.2476	0.9444	0.0000
	$\mathcal{D}_3$	0.00	0.00	0.00	0.00	0.00	0.00
	flow	0.0309	0.1006	0.0245	0.0208	0.0956	0.0622
Patient: $\mathcal{P}_2$	Ratio of $(c.o.v)_e$ w.r.t. $(c.o.v)_f$						
	$\mathcal{D}_1$	15.36	0.66	1.47	2.00	2.17	1.67
	$\mathcal{D}_2$	67.32	2.18	3.46	6.12	0.99	1.02
	$\mathcal{D}_3$	48.34	1.91	4.61	15.16	2.70	2.29
	Sample coefficients of variation						
	$\mathcal{D}_1$	0.3370	0.1000	0.2867	0.2161	0.4901	0.3643
	$\mathcal{D}_2$	1.4771	0.3283	0.6729	0.6615	0.2235	0.2214
	$\mathcal{D}_3$	1.0607	0.2873	0.8970	1.6382	0.6083	0.4984
	flow	0.0219	0.1506	0.1947	0.1080	0.2255	0.2180
Patient: $\mathcal{P}_3$	Ratio of $(c.o.v)_e$ w.r.t. $(c.o.v)_f$						
	$\mathcal{D}_1$	1.49	2.04	1.27	1.54	1.29	1.51
	$\mathcal{D}_2$	6.19	1.40	6.26	2.26	1.45	9.76
	$\mathcal{D}_3$	4.63	10.62	31.34	2.39	2.08	13.55
	Sample coefficients of variation						
	$\mathcal{D}_1$	0.2423	0.1703	0.0996	0.2588	0.2408	0.2728
	$\mathcal{D}_2$	1.0044	0.1173	0.4892	0.3799	0.2704	1.7634
	$\mathcal{D}_3$	0.7512	0.8866	2.4495	0.4015	0.3880	2.4495
	flow	0.1621	0.0835	0.0782	0.1680	0.1869	0.1808
Patient: $\mathcal{P}_4$	Ratio of $(c.o.v)_e$ w.r.t. $(c.o.v)_f$						
	$\mathcal{D}_1$	13.16	2.53	22.07	21.59	3.70	9.97
	$\mathcal{D}_2$	45.27	14.15	52.90	48.04	15.40	30.62
	$\mathcal{D}_3$	0.00	0.00	0.00	0.00	0.00	0.00
	Sample coefficients of variation						
	$\mathcal{D}_1$	0.1855	0.0483	0.7105	0.2151	0.0791	0.4511
	$\mathcal{D}_2$	0.6379	0.2697	1.7030	0.4786	0.3293	1.3856
	$\mathcal{D}_3$	0.00	0.00	0.00	0.00	0.00	0.00
	flow	0.0141	0.0191	0.0322	0.0100	0.0214	0.0452

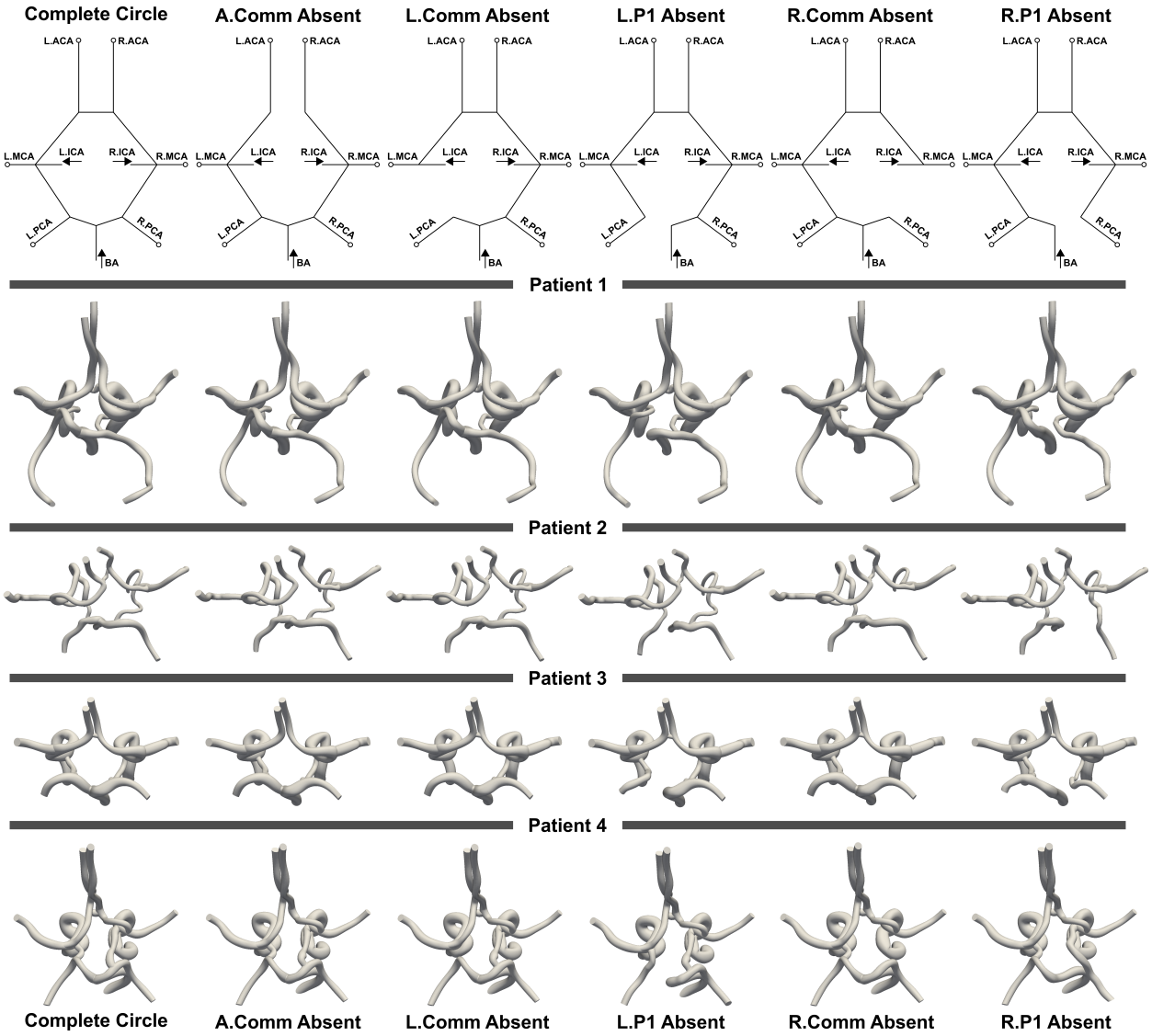

Figure 1: *An illustration of all the 24 different Circle of Willis anatomical models considered for this study. Note that the zoom and scale of each has been adjusted so that all of them fit the same width on this image-panel. Top row depicts schematic versions of the respective anatomical variant, with artery labels followed in the study. L/R denote left and right; ACA, MCA, PCA denote anterior, middle, and posterior cerebral arteries respectively; ICA is the internal carotid artery, and BA denotes the basilar artery.*

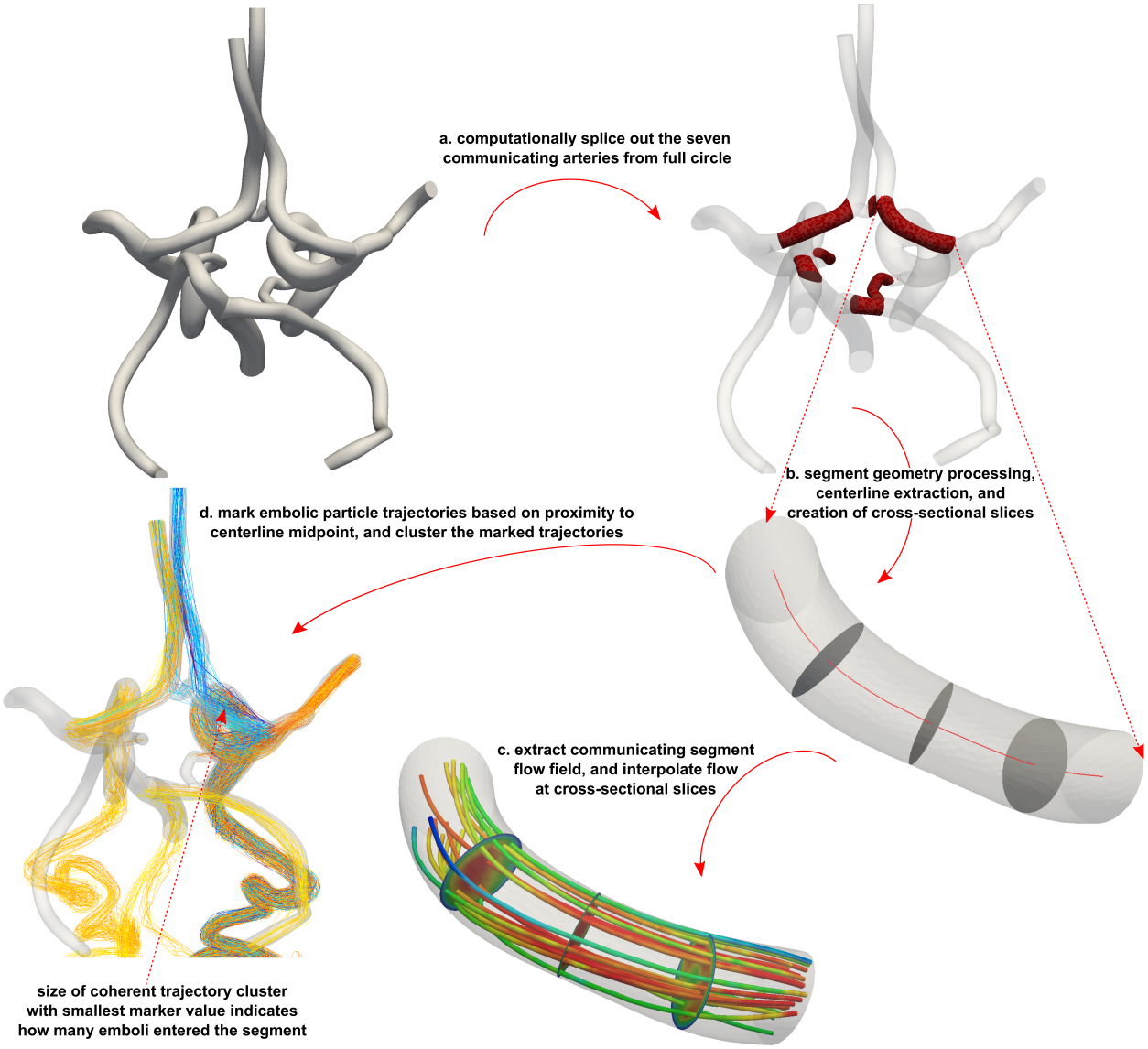

Figure 2: *A schematic illustration of the procedure to analyze the routing of flow, and embolus traversal, across the various artery segments of the Circle of Willis.*

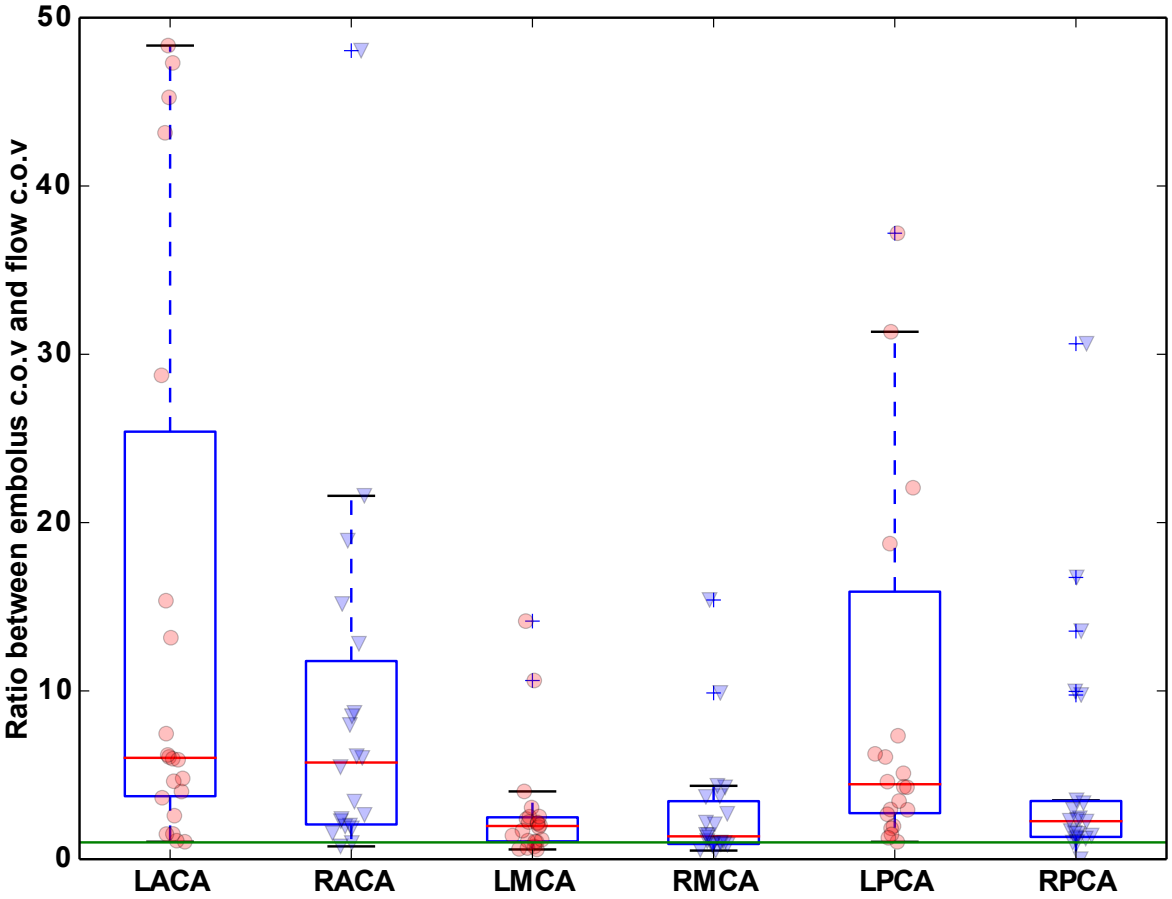

Figure 3: *Sample statistics for the ratio between the coefficient of variation for embolus distribution* $(c.o.v)_p$ *w.r.t that for flow distribution* $(c.o.v)_f$ *for each cerebral artery. A ratio of unity (the green solid line) indicates variability induced in embolus and flow distribution are equal, and values greater than unity denote that variability induced in embolus distribution is greater than that expected from flow alone.*

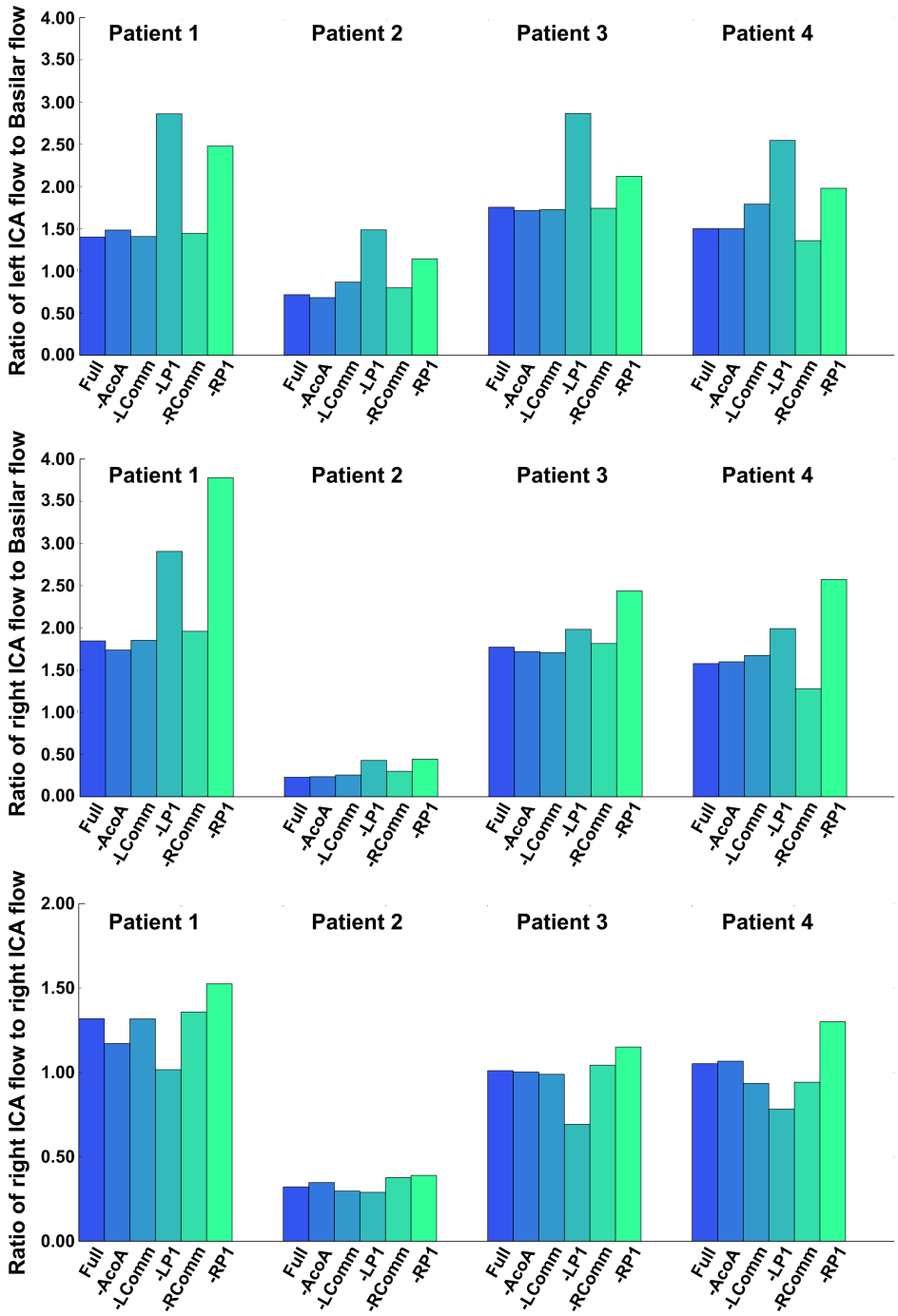

Figure 4: *The resulting ratios of incoming flow (into the brain) between (a) left internal carotid and basilar arteries (top); (b) right internal carotid and basilar arteries (mid); and (c) right and left internal carotid arteries (bottom); compared across all Circle of Willis anatomical variants considered, for all four patients.*

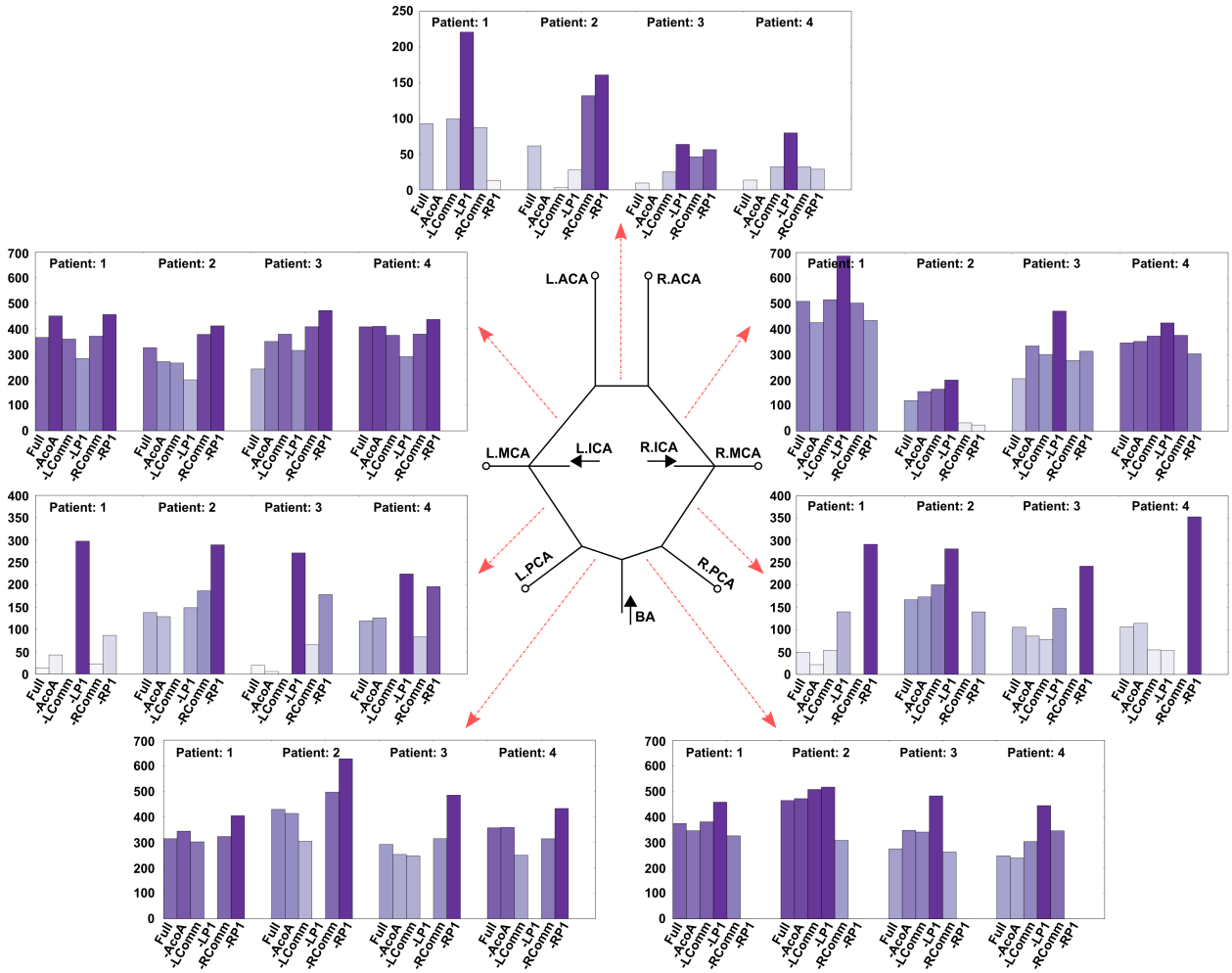

Figure 5: *Peak systolic flow through each communicating artery segment, compared across all Circle of willis anatomical variations, for each patient. The dotted lines indicate the artery segments that were absent in the anasotomoses considered.*

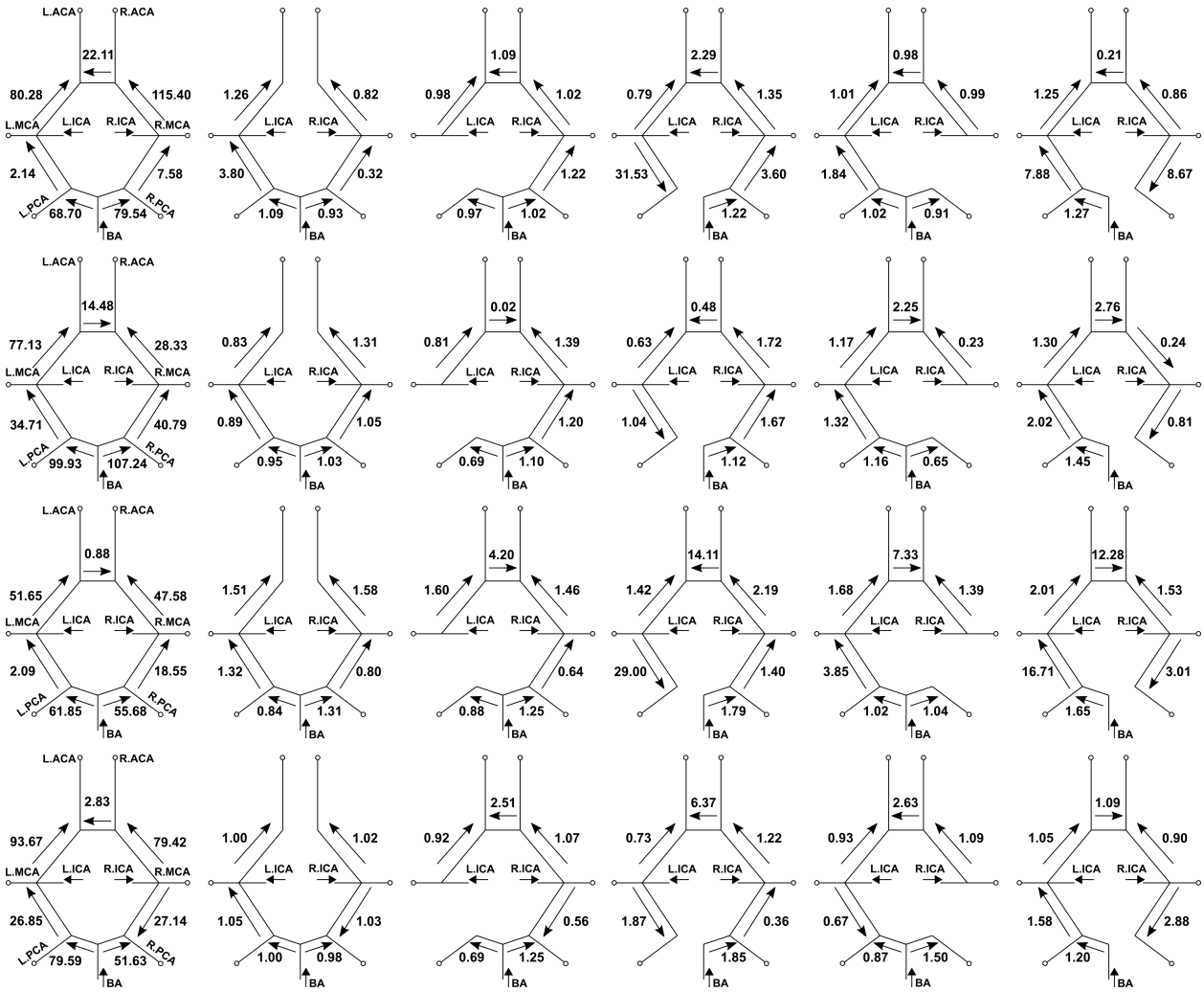

Figure 6: *Map showing recruitment patterns for the various communicating artery segments of the Circle of Willis, compared across each anatomical variant. Arrows indicate direction of average flow. The first model in each row denotes the total average flow rate (ml/min) and flow direction. The remaining five anatomical variants are annotated based on the factor by which the average flow rate changes when compared with the corresponding flow for the full Circle of Willis model.*

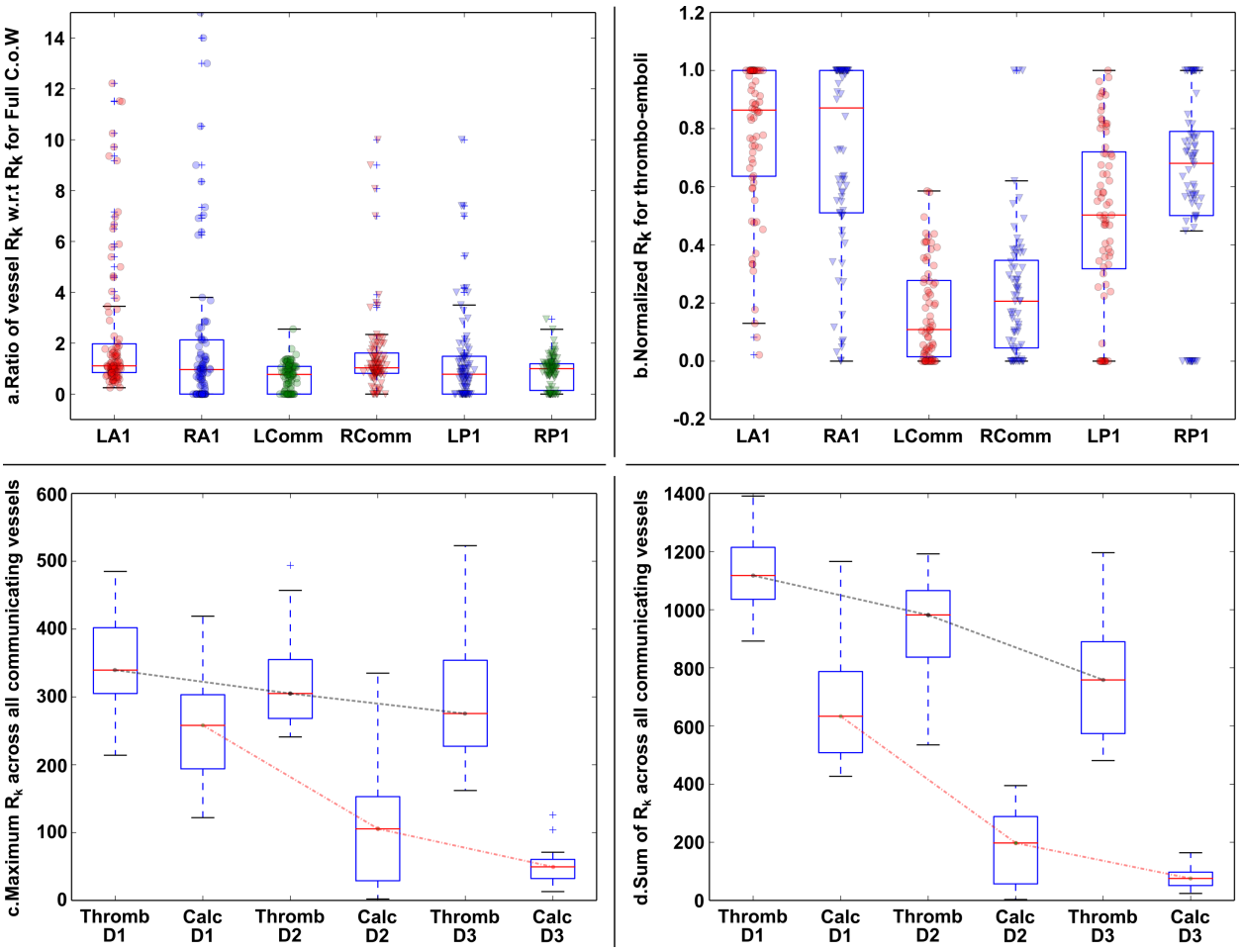

Figure 7: *Illustration of the results for embolus routing analysis. Panel a. depicts the ratios between the routing count (R_k) through each vessel ion a model, when compared with that of the same vessel for the full Circle of Willis model. Panel b. depicts the sample statistics for R_k for each vessel within a Circle of Willis anatomy normalized with respect to the maximum R_k observed for that anatomy. Panels c. and d. depict the variation in the extent of embolus traversal across the Circle of Willis (quantified by the maximum, and the total R_k values for each embolus type) with respect to embolus size and material composition. The two dashed lines indicate different material composition, and variations along each reflects the role of momentum response time of emboli.*

Supplementary Material

Suplementary Reference List For Choosing Circle Anatomy Models

[S**1**] J. Alastruey, K.H. Parker, J. Peiró, S.M. Byrd, and S.J. Sherwin. Modelling the circle of Willis to assess the effects of anatomical variations and occlusions on cerebral flows. *Journal of biomechanics*, 40(8):1794–1805, 2007.

[S**2**] B.J. Alpers, R.G. Berry, and R.M. Paddison. Anatomical studies of the circle of Willis in normal brain. *AMA Archives of Neurology & Psychiatry*, 81(4):409–418, 1959.

[S**3**] A. Bass, W.C. Krupski, R.B. Dilley, E.F. Bernstein, and S.M. Otis. Comparison of transcranial and cervical continuous-wave Doppler in the evaluation of intracranial collateral circulation. *Stroke*, 21(11):1584–1588, 1990.

[S**4**] S.K. Battacharji, E.C. Hutchinson, and A.J. McCall. The circle of Willis – the incidence of developmental abnormalities in normal and infarcted brains. *Brain*, 90(4):747–758, 1967.

[S**5**] R. Chaudhuri, T.S. Padayachee, R.R. Lewis, R.G. Gosling, and T.C.S. Cox. Non-invasive assessment of the circle of Willis using transcranial pulsed Doppler ultrasound with angiographic correlation. *Clinical radiology*, 46(3):193–197, 1992.

[S**6**] K.R.D. De Silva, R. Silva, D. Amaratunga, W.S.L. Gunasekera, and R.W. Jayesekera. Types of the cerebral arterial circle (circle of Willis) in a Sri Lankan population. *BMC neurology*, 11(1):5, 2011.

[S**7**] B. Eftekhar, M. Dadmehr, S. Ansari, M. Ghodsi, B. Nazparvar, and E. Ketabchi. Are the distributions of variations of circle of Willis different in different populations? – Results of an anatomical study and review of literature. *BMC neurology*, 6(1):22, 2006.

[S**8**] A. El Khamlichi, M. Azouzi, F. Bellakhdar, A. Ouhcein, and A. Lahlaidi. Anatomic configuration of the circle of Willis in the adult studied by injection technics. Apropos of 100 brains. *Neuro-Chirurgie*, 31(4):287–293, 1984.

[S**9**] E. Fawcett and J.V. Blachford. The circle of Willis: an examination of 700 specimens. *Journal of anatomy and physiology*, 40(Pt 1):63–2, 1905.

[S**10**] C.M. Fisher. The circle of Willis: anatomical variations. *Vasc Dis*, 2(99-105):15, 1965.

[S**11**] E. Harizi, A. Rroji, E. Cekaj, and S. Gabrani. Anatomical variations of the circle of Willis and cerebrovascular accidents in transitional Albania. *South Eastern European Journal of Public Health*, 3(1), 2015.

[S**12**] M.J. Hartkamp, J. van der Grond, K.J. van Everdingen, B. Hillen, and W.P.T.M. Mali. Circle of Willis collateral flow investigated by magnetic resonance angiography. *Stroke*, 30(12):2671–2678, 1999.

[S**13**] S.M. Hashemi, R. Mahmoodi, and A. Amirjamshidi. Variations in the anatomy of the Willis' circle: A 3-year cross-sectional study from Iran (2006-2009). are the distributions of variations of circle of willis different in different populations? result of an anatomical study and review of literature. *Surgical neurology international*, 4:65, 2013.

[S**14**] A.W.J. Hoksbergen, D.A. Legemate, D.T. Ubbink, and M.J.H.M. Jacobs. Collateral variations in circle of Willis in atherosclerotic population assessed by means of transcranial color-coded duplex ultrasonography. *Stroke*, 31(7):1656–1660, 2000.

[S**15**] S. Iqbal. A comprehensive study of the anatomical variations of the circle of Willis in adult human brains. *Journal of clinical and diagnostic research: JCDR*, 7(11):2423, 2013.

[S**16**] K. Kapoor, B. Singh, and Lt I.J. Dewan. Variations in the configuration of the circle of Willis. *Anatomical science international*, 83(2):96–106, 2008.

[S**17**] G. Lazorthes, A. Gouaze, J.J. Santini, and G. Salamon. Le cercle artériel du cerveau. *Anatomia Clinica*, 1:241–257, 1979.

[S**18**] C. Macchi, C. Catini, C. Federico, M. Gulisano, P. Pacini, F. Cecchi, L. Corcos, and E. Brizzi. Magnetic resonance angiographic evaluation of circulus arteriosus cerebri (circle of Willis): a morphologic study in 100 human healthy subjects. *Italian journal of anatomy and embryology= Archivio italiano di anatomia ed embriologia*, 101(2):115–123, 1995.

[S**19**] C. Malamateniou, M.E. Adams, L. Srinivasan, J.M. Allsop, S.J. Counsell, F.M. Cowan, J.V. Hajnal, and M.A. Rutherford. The anatomic variations of the circle of Willis in preterm-at-term and term-born infants: an MR angiography study at 3T. *American Journal of Neuroradiology*, 30(10):1955–1962, 2009.

[S**20**] V.N. Prasad, P.K. Chhetri, and A. Paudel. Normal variants of the circle of Willis in patients undergoing CT angiography. *Journal of College of Medical Sciences-Nepal*, 13(1):190–192, 2017.

[S**21**] A. Puchades-Orts, M. Nombela-Gomez, and G. Ortuño-Pacheco. Variation in form of circle of Willis: some anatomical and embryological considerations. *The Anatomical Record*, 185(1):119–123, 1976.

[S**22**] H.E. Riggs and C. Rupp. Variation in form of circle of Willis: the relation of the variations to collateral circulation: anatomic analysis. *Archives of Neurology*, 8(1):8–14, 1963.

[S**23**] K.W. Stock, S. Wetzel, E. Kirsch, G. Bongartz, W. Steinbrich, and E.W. Radue. Anatomic evaluation of the circle of Willis: MR angiography versus intraarterial digital subtraction angiography. *American journal of neuroradiology*, 17(8):1495–1499, 1996.

[S**24**] P.N. Tandon. Epidemiological study on subarachnoid haemorrhage in India (1972-75). *ICMR Bull*, pages 1–34, 1987.

[S**25**] S. Yaseen, Z.H. Riyaz, and A.A. Siddiqui. Variations in the brain circulation–the circle of Willis. *Indian Journal of Neurosciences*, 2(2):37–42, 2016.

Additional figures and animations

For additional visualization of data, we have included here a collection of figures which support and supplement the figures and data presented in the main manuscript. Furthermore, an animation has been included in the supplementary media, which illustrate the various key features of the embolus particle dynamics as they traverse a realistic patient arterial pathway.

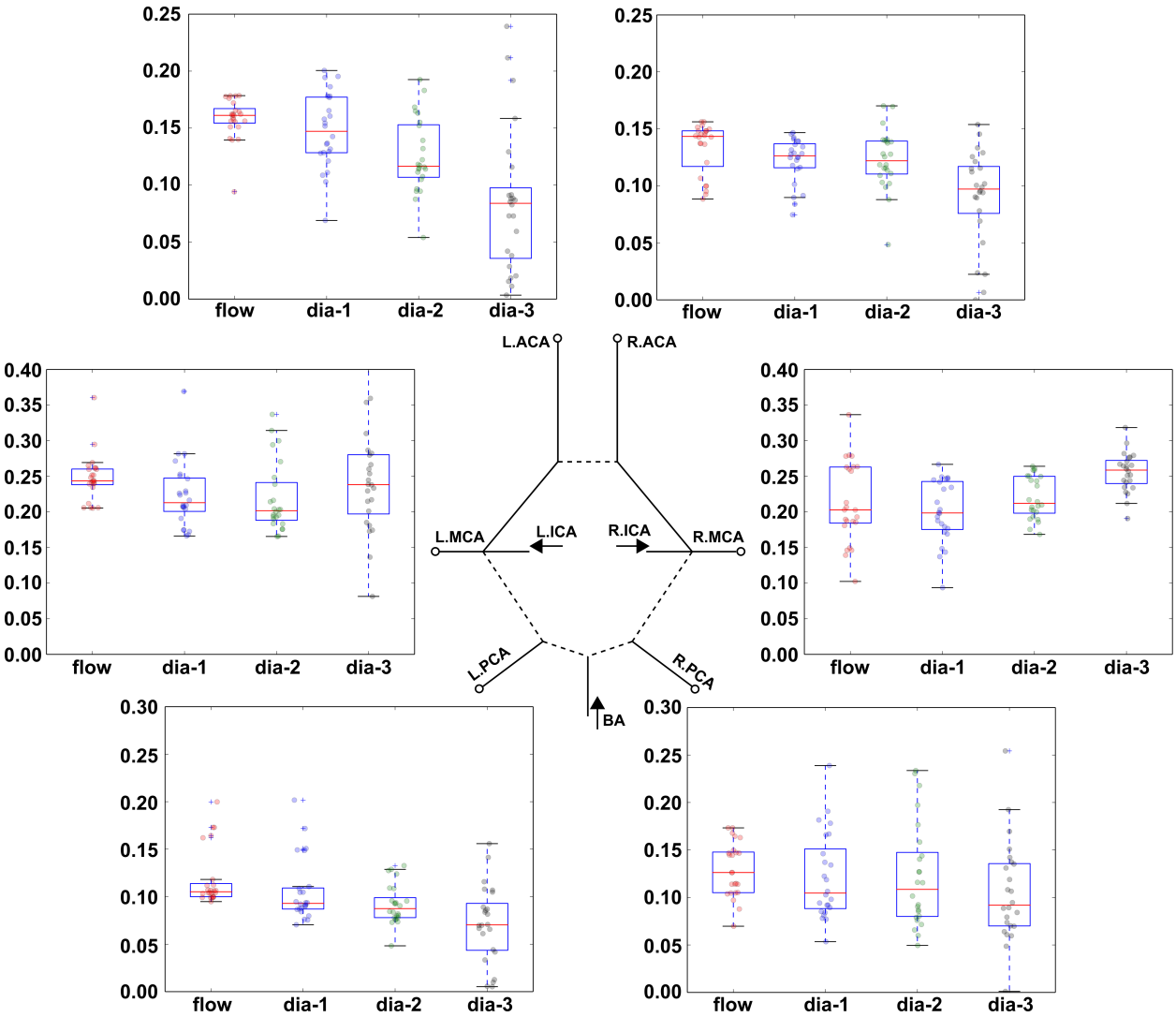

Figure S1: *A combined illustration of the distribution fractions of thrombo-emboli to each cerebral artery, as a function of embolus size, computed across all the Circle anatomical variations considered. The corresponding variabilities in flow distribution have also been included. These sample data correspond to the coefficient of variation ratios in Tables 2 and 3.*

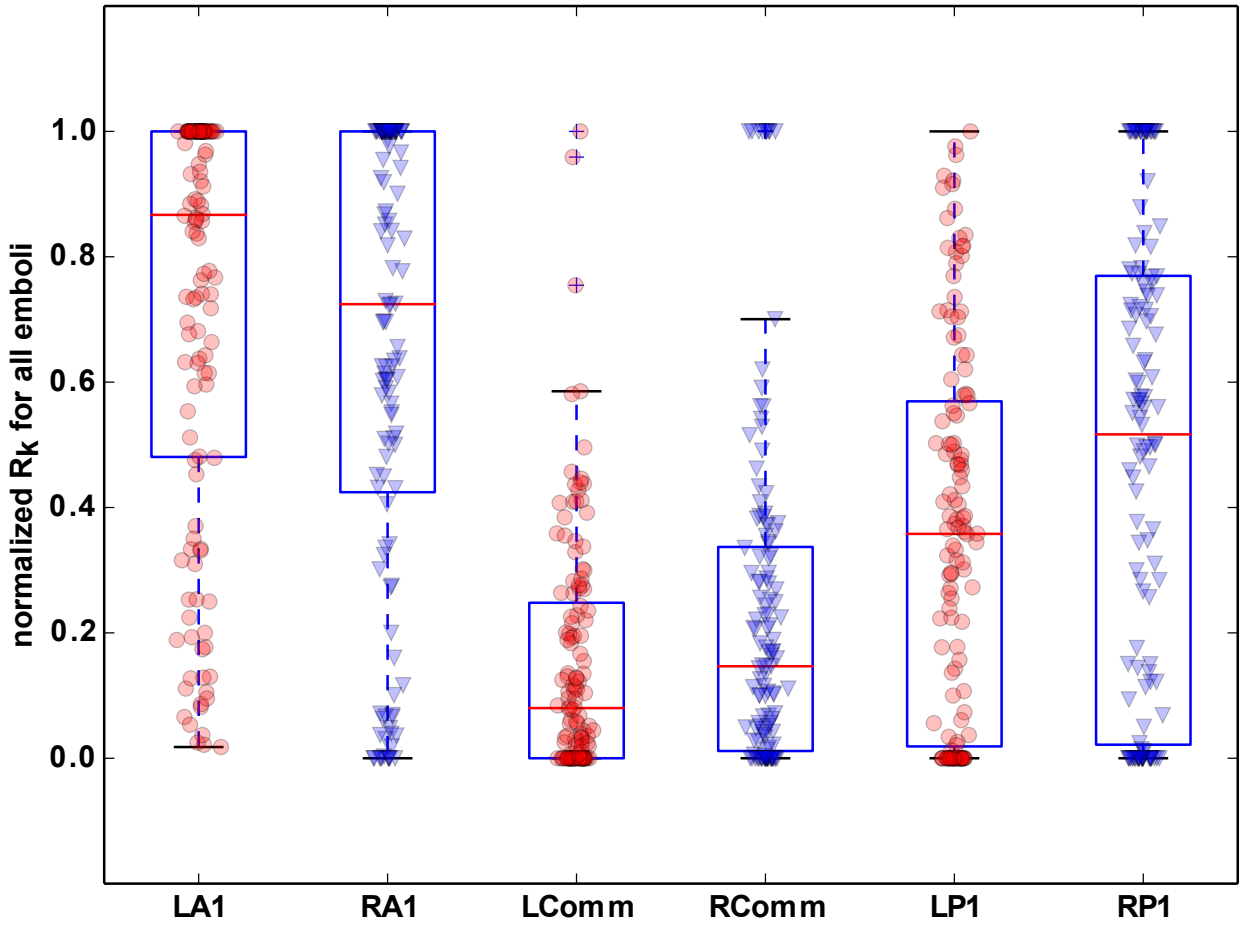

Figure S2: *Normalized routing count (R_k) values compiled for all the embolus sizes and material compositions considered, computed across all the Circle of Willis anatomical variations.*

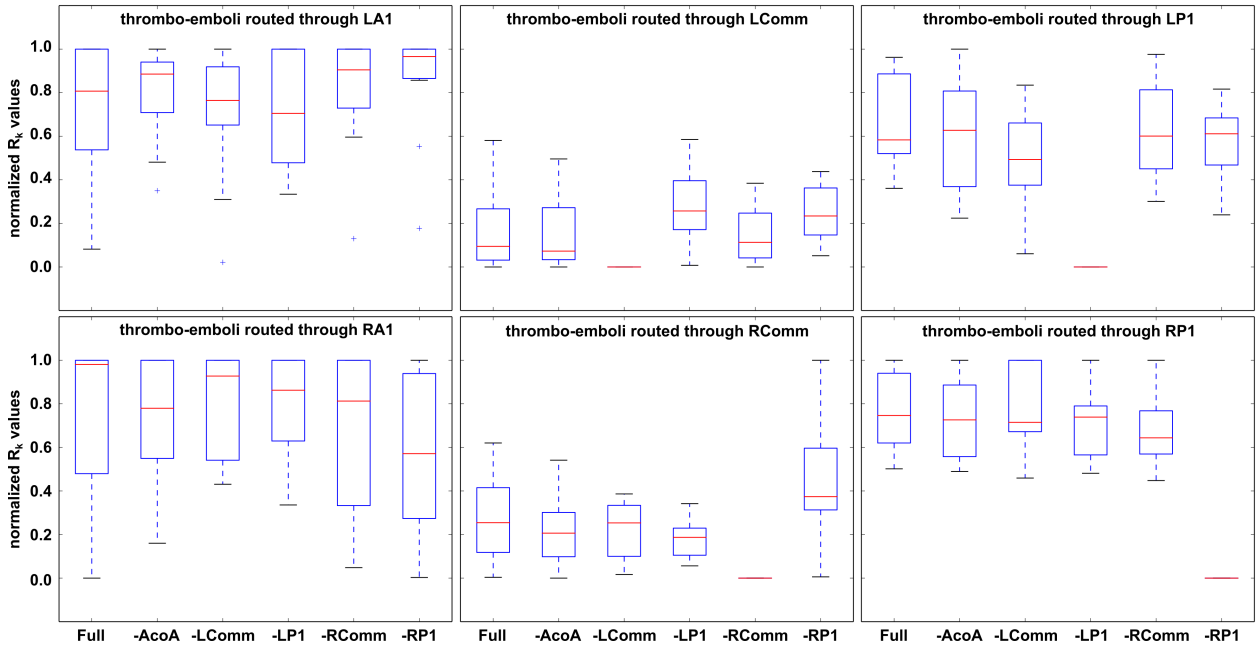

Figure S3: *Description of thrombo-embolus routing through the Circle of Willis for varying anastomoses, illustrated for each communicating artery segment (except the anterior communicating artery as described in Section 3.5).*

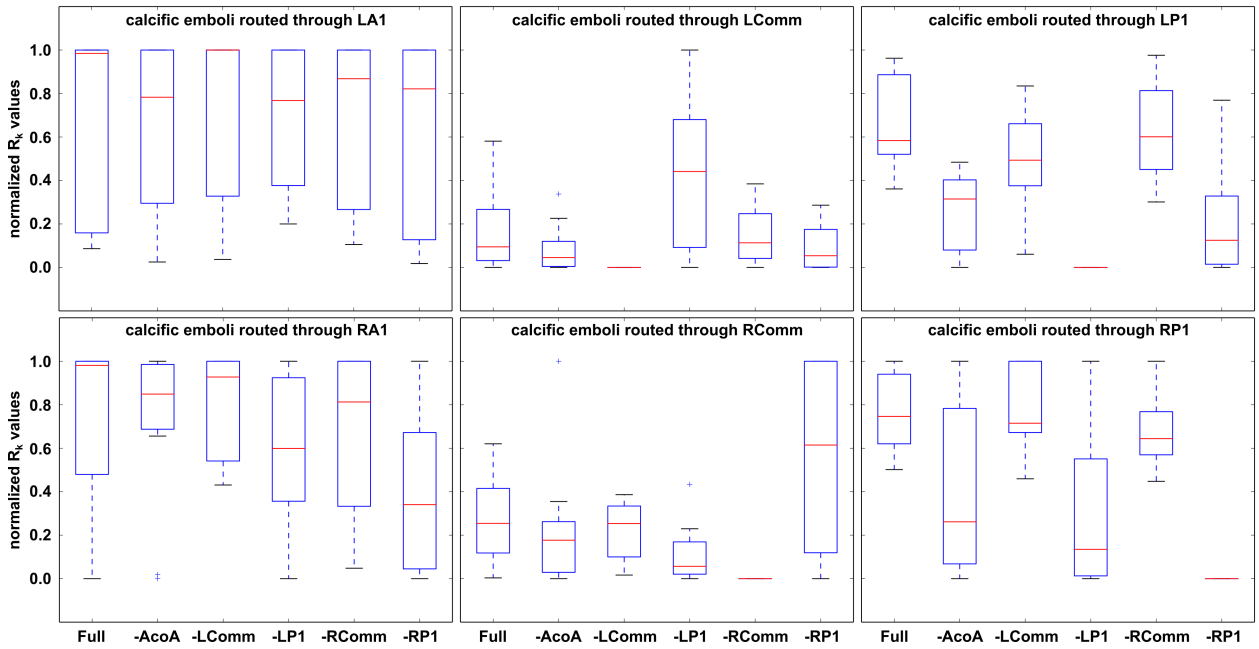

Figure S4: *Description of cacific-embolus routing through the Circle of Willis for varying anastomoses, illustrated for each communicating artery segment (except the anterior communicating artery as described in Section 3.5)*